ASPERA-4: Analyser of Space Plasmas and Energetic Atoms

S. Barabash[1], J.-A. Sauvaud[2], H. Gunell[1], H. Andersson[1], A. Grigoriev[1], K. Brinkfeldt[1], Y. Futaana[1], M. Holmström[1], R. Lundin[1], M. Yamauchi[1], K. Asamura[3], W. Baumjohann[4], H. Lummer[4], T. Zhang[4], A.J. Coates[5], D.R. Linder[5], D.O. Kataria[5], C.C. Curtis[6], K.C. Hsieh[6], B.R. Sandel[6], A. Fedorov[2], C. Mazelle[2], J.-J. Thocaven[2], M. Grande[7], H.E.J. Koskinen[8, 9], E. Kallio[9], T. Säles[9], W. Schmidt[9], P. Riihela[9], J. Kozyra[10], N. Krupp[11], M. Fränz[11], J. Woch[11], J. Luhmann[12], S. McKenna-Lawlor[13], S. Orsini[14], R. Cerulli-Irelli[14], A. Mura[14], A. Milillo[14], M. Maggi[14], E. Roelof[15], P. Brandt[15], C.T. Russell[16], K. Szego[17], J.D. Winningham[18], R.A. Frahm[18], J. Scherrer[18], J.R. Sharber[18], P. Wurz[19] & P. Bochsler[19]

[1]*Swedish Institute of Space Physics, Box 812, SE-981 28 Kiruna, Sweden*
Email: stas@irf.se
[2]*Centre d'Etude Spatiale des Rayonnements, BP-4346, F-31028 Toulouse, France*
[3]*Institute of Space and Astronautical Science, 3-1-1 Yoshinodai, Sagamichara, Japan*
[4]*Space Research Institute, Schmiedlstr. 6, A-8042 Graz, Austria*
[5]*Mullard Space Science Laboratory, University College London, Surrey RH5 6NT, UK*
[6]*University of Arizona, Tucson, AZ 85721, USA*
[7]*University of Wales, Aberystwyth, Penglais, Aberystwyth, Ceredigion, SY23 3BZ, UK*
[8]*University of Helsinki, Department of Physical Sciences, P.O. Box 64, FIN-00014 Helsinki, Finland*
[9]*Finnish Meteorological Institute, Box 503 FIN-00101 Helsinki, Finland*
[10]*Space Physics Research Laboratory, University of Michigan, Ann Arbor, MI 48109-2143, USA*
[11]*Max-Planck-Institut für Sonnensystemforschung, D-37191 Katlenburg-Lindau, Germany*
[12]*Space Science Laboratory, University of California at Berkeley, Berkeley, CA 94720-7450, USA*
[13]*Space Technology Ireland, National University of Ireland, Maynooth, Co. Kildare, Ireland*
[14]*Instituto di Fisica dello Spazio Interplanetari, I-00133 Rome, Italy*
[15]*Applied Physics Laboratory, Johns Hopkins University, Laurel, MD 20723-6099, USA*
[16]*Institute of Geophysics and Planetary Physics, University of California, 405 Hilgard Ave., Los Angeles CA 90095-1567, USA*
[17]*KFKI Research Institute for Particle and Nuclear Physics, H-1525, Box 49, Budapest, Hungary*
[18]*Southwest Research Institute, San Antonio, TX 7228-0510, USA*
[19]*University of Bern, Physikalisches Institut, CH-3012 Bern, Switzerland*

The general objective of ASPERA-4 (Analyser of Space Plasmas and Energetic Atoms) is to study the solar wind-atmosphere interaction and characterise the plasma and neutral gas environment in near-Venus space through energetic neutral atom (ENA) imaging and local charged particle measurements. The studies address the fundamental question: how strongly do the interplanetary plasma and electromagnetic fields affect the atmosphere of Venus? ASPERA-4 comprises four sensors: two ENA sensors, and electron and ion spectrometers. The Neutral Particle Imager (NPI) measures the integral ENA flux (0.1–60 keV) with no mass or energy resolution but relatively high angular resolution. The Neutral Particle Detector (NPD) measures the ENA flux, resolving velocity (0.1–10 keV for hydrogen) and mass (H and O) with a coarse angular resolution. The electron spectrometer (ELS) is a standard top-hat electrostatic analyser (energy range 0.001–20 keV) in a very compact design. These three sensors are on a scanning platform providing 4π coverage. ASPERA-4 also contains an ion mass composition sensor, IMA (Ion

Mass Analyser). Mechanically, IMA is a separate unit electrically connected to the ASPERA-4 main unit. IMA provides ion measurements in the energy range 0.01–36 keV/*q* for the main ion components H^+, He^{++}, He^+, O^{++}, O^+ and CO_2^+ ion group with $M/q > 40$ amu/*q*.

1. The Science

1.1 Scientific objectives for plasma measurements at Venus

Venus, Earth and Mars, the three largest terrestrial planets, have undergone very different thermal and atmospheric evolutions. Mars has evolved rapidly. Initially, it is now believed, Mars had a strong internally driven magnetic shield over an atmosphere much denser than present, possibly supporting rain and flowing water on the surface. The interior then cooled rapidly, the dynamo stopped and much of the atmosphere escaped (Acuna et al., 1998; Schubert et al., 2000). In contrast, Earth still has its magnetic field, a substantial atmosphere and abundant water. Venus may be the least evolved of the three planets. A thick crust has kept the interior hot but, at the same time, stifled the heat flow needed to drive convection in the fluid iron core. Thus Venus has no magnetic shield against the solar wind and perhaps never had (Russell et al., 1980). Venus has a very dense atmosphere but very little water. Clearly, the atmosphere has evolved greatly since the planet accreted, yet much atmosphere remains. Possibly the escape mechanism is very selective, favouring the escape of water or perhaps hydrogen, leaving the oxygen to combine with the soil. It is not known because no mission to Venus has been instrumented to address this objective. Therefore, the main scientific objective of the ASPERA-4 (Analyser of Space Plasmas and Energetic Atoms) instrument is to study solar wind-induced atmospheric escape. The specific scientific questions to be addressed are:

- how is the atmosphere coupled with the solar wind? How is mass added to and removed from the atmosphere owing to this coupling?
- what is the structure of the interaction region?
- the previous question is connected to the issue of 'where did the water go?' The early atmosphere must have contained water equivalent to a global ocean a few metres deep, inferred from the H/D ratio (Donahue & Hartle, 1992). Could the solar wind interaction have contributed to the water escape (mainly increasing the escape of H)? Is the process the same as for the water escape from Mars?
- what is the mass composition of the escaping plasma? To what degree are the outflow processes mass-dependent, and can it explain the loss of water and greenhouse effect?
- what is the neutral-plasma interaction on Venus? How does the presence of the neutral gas affect plasma dynamics?
- what are the similarities and differences in the solar wind interaction with the other terrestrial planets?

No previous mission to Venus has covered such a wide range of scientific objectives. ASPERA-4 is a replica of the ASPERA-3 instrument orbiting Mars aboard the Mars Express mission (Barabash et al., 2004). Combining the observations made by two identical instruments at two non-magnetised planets exhibiting similar solar wind interaction but differing significantly in terms of interplanetary conditions, atmospheric characteristics and size and mass provides a completely new perspective for comparative magnetospheric studies.

1.2 Required measurements

In order to study the escape of today's atmosphere, the incident solar wind flux and the escaping ions (with thermal and bulk velocities of about 10–1000 km/s,

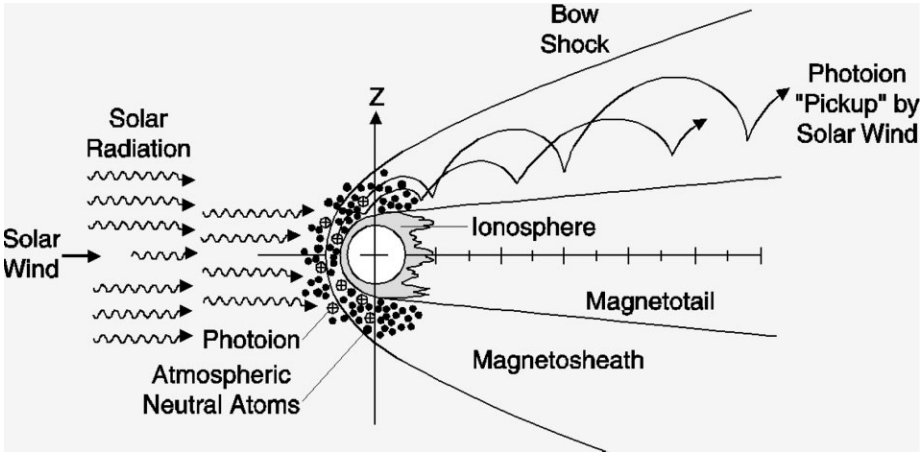

Fig. 1. The Venus-solar wind interaction, highlighting the atmosphere escape processes connected with the generation of O^+ pickup ions. Solar radiation ionises the atmosphere, producing an ionosphere with sufficient thermal pressure to hold off the solar wind flow, bounding the ionosphere with an ionopause. The deflection of the supersonic solar wind leads to the formation of a bow shock. The hydrogen and hot oxygen exospheres extend into the shocked solar wind of the magnetosheath, where they are photoionised and impact-ionised and picked up in cycloidal trajectories gyrating around the magnetic field (out of the page).

depending on the mechanism at work) must be measured. Since O_2^+ ions dissociatively recombine to form a hot oxygen corona out to 4000 km altitude, oxygen ions originating from the corona are picked up in the solar wind as well as accelerated down the wake or tail of Venus on the nightside. Charge exchange between the solar wind and the neutral Venus atmosphere should be an important process because of the dense upper atmosphere. Thus energetic neutral atoms (ENAs; Gunell et al., 2005c) and possibly X-rays (Holmström et al., 2001) will be generated. This opens up the possibility of imaging the interaction region to obtain instantaneous images of the global distribution of the solar wind and planetary plasmas to qualify the instantaneous escape induced by the solar wind. These measurements need to detect both hydrogen and oxygen atoms at speeds near 400 km/s. Estimates of the ion loss rate are around 10^{24} ions/s (Moore et al., 1991). Ion and ENA measurements should be supported by the electron measurements to characterise the local plasma conditions and identify the main plasma domains. ASPERA-4 thus includes four sensors: the Electron Spectrometer (ELS), the Ion Mass Analyser (IMA), the Neutral Particle Imager (NPI) and the Neutral Particle detector (NPD).

In order to characterise the environment of the pick-up ions and understand the mechanism involved in their acceleration, the magnetic field must be measured. The ambient magnetic field ranges from about 1 nT to 200 nT but more typically 10 nT to 30 nT. Since the spacecraft carries some magnetic field, a range of up to 1000 nT is recommended using gradiometer sensors along a modest (0.5 m long) boom with monitoring of current levels of critical sources of stray magnetic fields. The MAG magnetometer is included in the Venus Express payload (Zhang et al., 2005).

1.3 The solar wind-atmosphere interaction

Near-Venus space is strikingly different from Earth-space because of the absence of a substantial intrinsic magnetic field. Without the magnetic cavity of a magnetosphere to shield the upper atmosphere from the oncoming solar wind, Venus is subjected to comet-like atmosphere erosion processes and solar wind-induced current systems that have no terrestrial counterparts. Data from the Pioneer Venus Orbiter (PVO) have helped to develop ideas of how the upper atmosphere and solar wind interact and the consequences for the planet. In particular, it has been observed that the scavenging of planetary ions removes heavy constituents such as oxygen, which plays an important role in the atmosphere's hydration and surface oxidation history. Some of the processes are shown in Fig. 1.

The current atmospheric conditions on Venus indicate that water is present in

only trace amounts (a few precipitable micrometres), much less than expected if the early atmosphere was Earth-like. In contrast to the story of water on Mars (McKay & Stoker, 1989), it is unlikely to be frozen and buried or sequestered in polar ice caps. Thus the alternative of escape to space in the form of water's constituents is most likely. It is relatively easy to lose light hydrogen, but oxygen loss is problematic. Small amounts can escape via the production of a hot atomic oxygen corona from ionospheric photochemistry (Nagy et al., 1981), but the bulk of the O_2 and O are gravitationally bound. Independent analyses of surface oxidation on the planet indicate that most of the oxygen left over from photodissociation over the history of Venus did not become incorporated into the exposed rocks and soil. What could produce such an effective oxygen escape mechanism? Could the processes associated with the solar wind interaction account for the escape of sufficient quantities of oxygen to have destroyed the Earth-like water budget of Venus 4 Gyr ago?

Each of ASPERA-4's four sensors contributes, both alone and in combination, to understanding the different consequences of direct solar wind interaction with a planetary atmosphere/ionosphere. Since Venus does not have the complication of the Martian remanent magnetic fields, the ASPERA-4 measurements will fill in the knowledge gaps left from PVO's comprehensive reconnaissance and help to make progress in our understanding far exceeding its own coverage of the Venus-solar wind interaction physics. In particular, IMA places a definitive composition label on the atmospheric pickup ions produced at Venus and detects them over a much greater (up to 36 keV, as opposed to PVO's 8 keV) energy range. ELS measures both low-energy escaping plasma and high-energy electrons that contribute to the ion production through electron impact ionisation. The ENAs detected by NPD and NPI provide a measure of solar wind energy deposited in the atmosphere that cannot be estimated from the plasma and field measurements alone, as described below.

A combination of PVO results led to the current picture of atmospheric oxygen escape from Venus, depicted in Fig. 1. The UV spectrometer (Stewart, 1980) confirmed the existence of an atomic oxygen upper atmosphere extending well into the magnetosheath. This hot O 'corona' was shown by Nagy et al. (1981) to agree with models of photochemical exospheres produced by dissociative recombination in the O_2^+ ionosphere. Combined magnetometer (Russell et al., 1980) and plasma analyser (Intriligator et al., 1980; Mihalov et al., 1980) measurements were then used to construct a scenario of both direct O^+ pickup ion escape (Moore et al., 1990) and additional sputtering of O from the atmosphere by impacting O^+ pickup ions not on direct escape trajectories (Luhmann & Kozyra, 1991). The pickup ions can be created by any ionisation mechanism – photoionisation, solar wind electron impact or charge exchange with solar wind protons – in all atmospheric regions above the exobase (200 km altitude) penetrated by the solar wind convection electric field. There are also suggestions of other possible ion removal processes in the thermal plasma (below a few eV) energy range at work at the ionopause boundary layer (Brace et al., 1982) and in the low-altitude wake (Hartle & Grebowsky, 1990), distinct from the pickup ion-related mechanisms, which are not discussed here. In any case, the limited capabilities of the PVO instruments for measuring solar wind electrons and magnetosheath protons (where the upper atmosphere penetration occurs), as well as solid identification of the pickup ion composition, made it difficult to quantify the details of the escape scenario in Fig. 1. The ASPERA-4 IMA, with the MAG magnetometer, on Venus Express should finally allow the evaluation of escape rates for oxygen ions and other species, their variation with interplanetary conditions, and their implications for related sputtering losses.

Another problem of the solar wind-atmosphere coupling that has not been explored experimentally concerns the energetic consequences for the atmosphere of the lack of a planetary dipole field of any importance. Kinetic and test-particle

models of the Mars-solar wind interaction (Brecht, 1997; Kallio et al., 1997) suggest that solar wind absorption by the Martian atmosphere may be an important energy source for the upper atmosphere at that planet. However, at Venus the much smaller relative solar wind proton gyroradii greatly limit the numbers of protons that can reach the exobase, which is well below the ionopause (200 km exobase altitude compared to 300 km ionopause altitude. A solar wind proton gyroradius in the inner magnetosheath is typically 10 km). ENA production in the magnetosheath by charge exchange between solar wind protons and the exosphere/thermosphere near the solar wind/ionosphere boundary decouples the energetic neutralised protons from the magnetic field in the sheath, leaving them free to impact the exobase (e.g. Kallio et al., 1997). The ENAs generated as a product of the solar wind interaction can thus greatly enhance the deposition of solar wind energy into the upper atmosphere (Kallio & Barabash, 2000) and, at the same time, provide a means of 'imaging' the solar wind interaction. Fok et al. (2004) and Gunell et al. (2005b) modelled the ENA production at Venus using magnetohydrodynamic (MHD) simulations. The NPD will provide tests of the predicted fluxes and composition of the ENAs, while imaging these particles with NPI will show the spots or regions of the most intense ENA precipitation, and give information on their variation with solar wind conditions.

While the energy transfer associated with the ENA precipitation can be important for the thermal structure of the upper atmosphere, it is the O^+ pickup ion precipitation that causes significant sputtering-induced loss of the atmosphere. Luhmann & Kozyra (1991) estimated that O^+ sputtering results in the escape of oxygen atoms from Venus at rates comparable to sputtering losses from the much smaller Mars (Luhmann & Bauer, 1992). Comparisons of ASPERA-3 results from Mars Express with ASPERA-4 results will provide an invaluable look at the processes and rates by which unmagnetised terrestrial planet atmospheres evolve through their solar wind interactions.

1.4 Pickup ions at Venus

Observations of oxygen pickup ions by the PVO Plasma Analyser (PV OPA) sparked broad interest in solar wind erosion of unmagnetised planet atmospheres with its first-order picture of the spatial distribution and energies of O^+ pickup ions. These results, collected during PVO's 14-year, 5000-orbit tour, provide an idea of what is to be expected from IMA measurements on Venus Express.

The PV OPA has been described in the literature (Intriligator et al., 1980; Mihalov & Barnes, 1982; Moore et al., 1990). Its key features included its 8 keV/q energy per charge upper limit for detection, and a directional sampling scheme, providing ~15° azimuthal and 20–30° polar angle resolution with respect to the PVO spin axis. The time resolution for a full angle and energy scan was about 9 min, which gave only a few samples during each periapsis pass. Thus the best

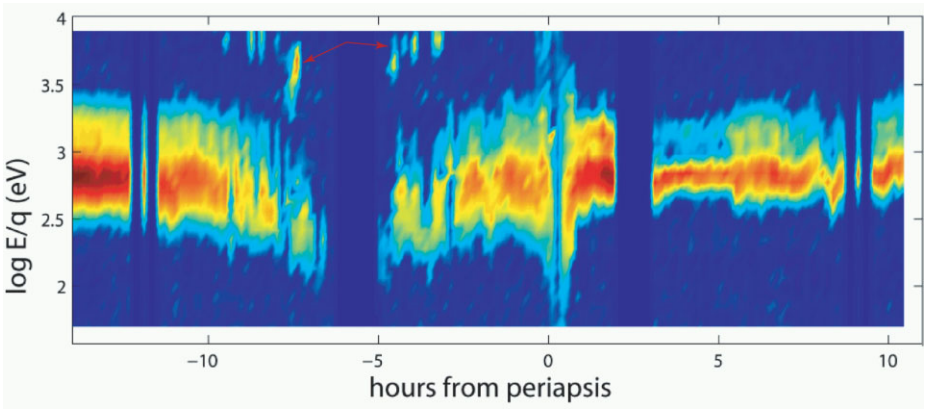

Fig. 2. Sample energy spectrogram obtained from the PVO plasma analyser data. The inferred O^+ is seen as the higher energy peak (arrowed) coexisting with the main proton peak.

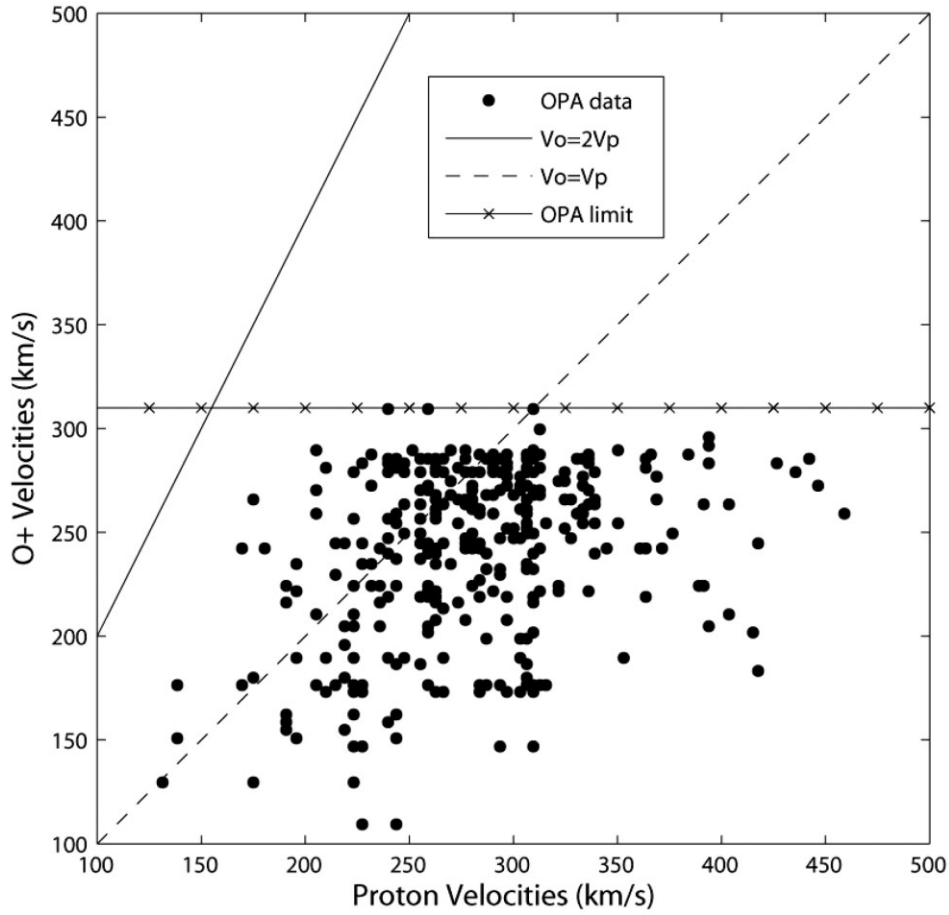

Fig. 3. Relative energies of the detected proton peaks and oxygen peaks in the PV OPA *E*/*Q* spectra. PV OPA has an 8 keV *E*/*q* limit for O^+ detection.

observations of pickup ions were generally obtained during apoapsis at about 12 planetary radii downstream. A sample of a spectrogram constructed from the PV OPA measurements during one orbit in which picked up ions were observed in the wake is shown in Fig. 2 (a typical orbit is shown in Fig. 4). O^+ ions are inferred to be present in the PV OPA energy scans when a second peak is visible at high *E*/*q*. The energy and angular coverage limitation implies that a significant amount of the O^+ present was not detected on PVO.

The energies and orbital locations of the oxygen peaks differ from orbit to orbit owing to the variability of the solar wind and especially the cross-flow interplanetary magnetic field orientation. The latter creates changing asymmetries in the O^+ spatial distribution owing to the large gyroradii of O^+ ions (~0.5–1.0 Venus-radius) relative to the size of the planet and the solar wind interaction region, as illustrated in Fig. 1. Because the direction of the interplanetary magnetic field is usually eastward or westward, the convection electric field $E = -v \times B$ (where v is the solar wind plasma velocity and B the local magnetic field) produces pickup ion trajectories that are initially either northward or southward as well as anti-Sunward. If the ion trajectory does not intersect the exobase at a few hundred kilometres altitude, the trajectory continues down the wake, forming a one-sided ion stream. Thus near the planet terminator and in the near-planet wake, O^+ detection locations organised into northern or southern spatial clusters are typically observed (Intriligator et al., 1979; Moore et al., 1990).

The energies at which the inferred O^+ ions were detected on PVO are compared with their accompanying proton peak energies in Fig. 3. At 16 times the proton mass, co-moving O^+ ions have 16 times the proton energies. The

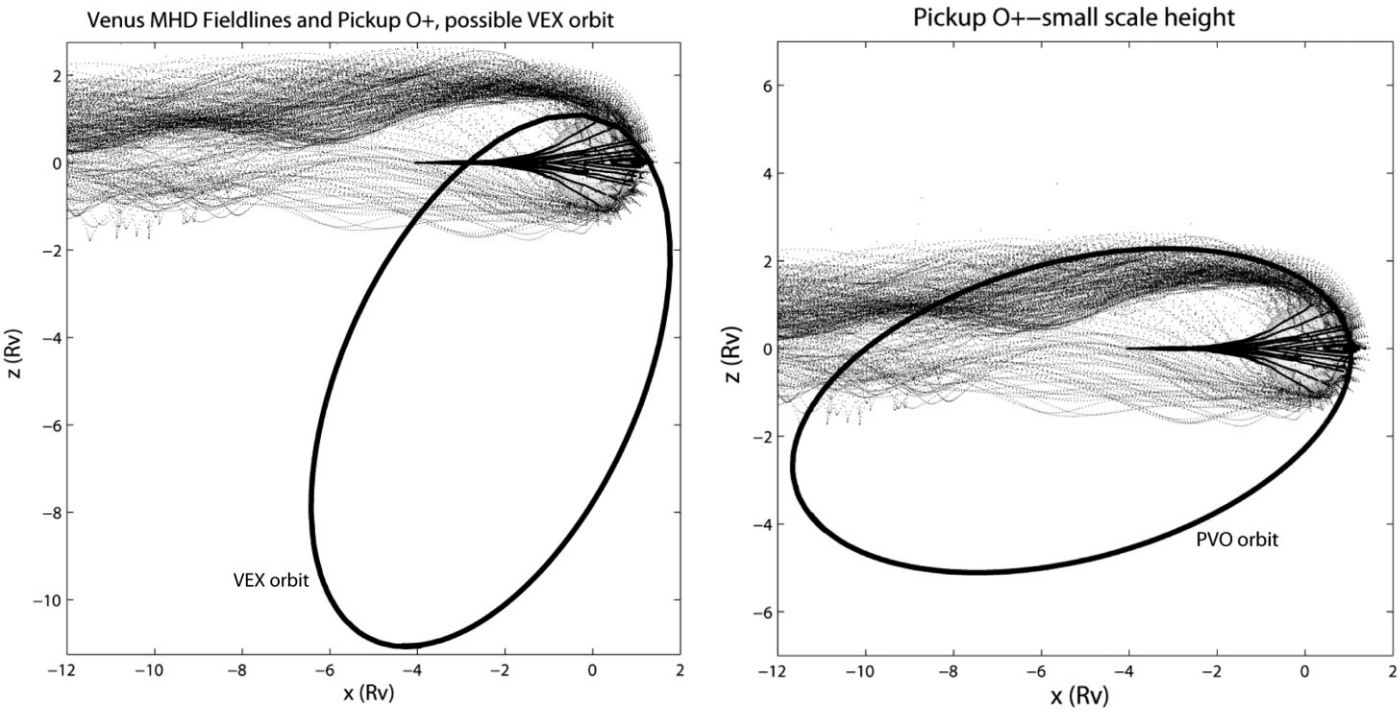

Fig. 4. Left: the planned Venus Express orbit, with periapsis at ~65ºN latitude, relative to O^+ ion test particle trajectories for a particular interplanetary field orientation. The sampling of the pickup ion population is advantageous for near-planet pickup studies. Right: the equivalent illustration for the PVO orbit, which, in contrast, sampled the deep ion wake.

statistics suggest the detected O^+ peaks are at roughly these energies up to the 8 keV limit of the PV OPA. O^+ moving at greater than ~310 km/s are outside of this range. In the upstream solar wind, outer magnetosheath and distant wake, the solar wind plasma often moves at speeds of 350 km/s to over 600 km/s. IMA on Venus Express can not only detect but also verify the composition of many of these additional O^+ (and other) pickup ions.

The PVO results suggest the extent to which ASPERA-4 on Venus Express, with its energy range of 10 eV to 36 keV, scanning field of view and ability to separate ion masses, will greatly improve our view of the pickup ion environment around the planet. The Venus Express orbit is similar to that of PVO, but with periapsis at ~65ºN and a periapsis of 250–400 km, compared to PVO's 15ºN initial periapsis and nominal ~160 km periapsis. The sampling of the pickup ion cloud in an orbit with this geometry, compared to the PVO orbit geometry that produced the spectrogram in Fig. 2, is illustrated in Fig. 4. The Venus Express orbit thus provides a somewhat different perspective, focusing on the magnetosheath, near-terminator and low-altitude wake pickup ion characteristics, rather than on the distant pickup ion wake characteristics. This is highly complementary to the PVO orbit geometry sampling, which did not allow coverage of the low-altitude wake. If the orbit is allowed to evolve so that the sampling region circularises, a broader sampling will be obtained.

1.5 ENA production at Venus

ENAs are produced in charge exchange collisions between solar wind protons and neutral atoms in the upper part of planetary atmospheres. ASPERA-4 provides ENA images of the Venus-solar wind interaction region. Such images were simulated through the integration of ENA production along lines-of-sight to a virtual ENA instrument (Fok et al., 2004; Gunell et al., 2005b). Some of the results from these simulation studies are reviewed here.

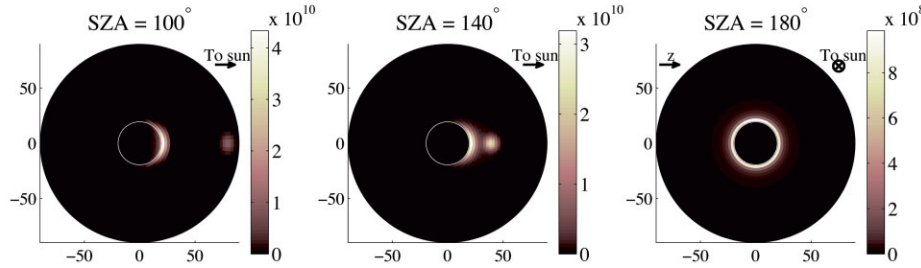

Fig. 5. ENA images of Venus from vantage points 3 R_V from Venus (planetocentric distance) and solar zenith angles θ = 100º, 140º and 180º. The ENA flux is shown in units of m^{-2} sr^{-1} s^{-1}, and the axes show the polar angle in degrees.

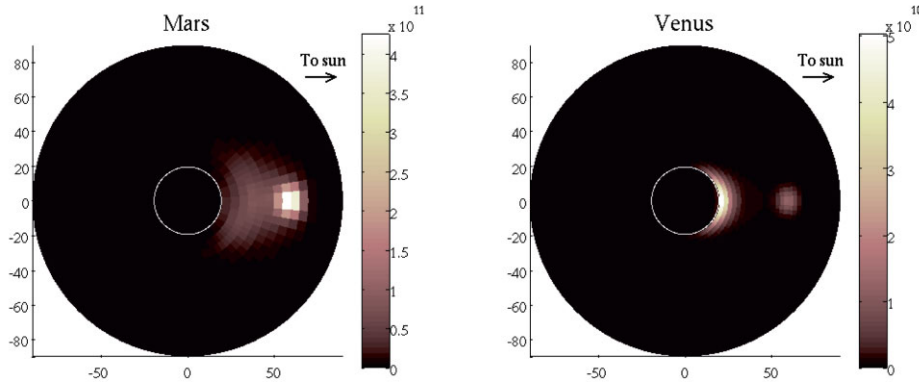

Fig. 6. ENA images of Mars and Venus from vantage points with solar zenith angles of 120º and planetocentric distances of three radii. The image of the Martian environment (Gunell et al., 2005b) is based on an MHD model of the plasma flow around Mars.

Venus Express arrived at the planet during solar minimum conditions. Owing to the scarcity of *in situ* measurements, the ionopause altitude at Venus is not well known for solar minimum conditions (Luhmann, 1992). It is thought to vary with the solar cycle, but since all *in situ* measurements were made during solar maximum conditions, this variation is unconfirmed.

Gunell et al. (2005b) investigated the ENA emissions as a function of ionopause distance by scaling the ionopause altitude in the plasma model. The ENA flux from the local emission maximum near the planet decreases with increasing ionopause altitude, since with a higher ionopause altitude the protons pass through a region with lower neutral density. This also affects the ENA production and escape rates. The ionopause is thought to be close to the lower end of that range at solar minimum because of the lower ionospheric pressure (Luhmann, 1992). The ENA images are then generated by evaluating line-of-sight integrals in the same way as was done for the Martian environment (Gunell et al., 2005a; Holmstrom et al., 2002). Gunell et al. (2005b) used a semi-analytical MHD model (Biernat et al., 1999; 2000; 2001) to describe the plasma flow around Venus, and a neutral gas density model that is based on published data from measurements. The input parameters were: solar wind density n_{sw} = 15 cm^{-3}; solar wind speed v_{sw} = 440 km/s; solar wind temperature T_{sw} = 2x10^5K; solar wind magnetic field B_{sw} = 12 nT. Three ENA images from vantage points in the xz-plane at different solar zenith angles are shown in Fig. 5. The vantage points are located three Venus radii from the centre of the planet, and the solar zenith angles are 100º, 140º and 180º for the three images, respectively.

The centre of each image corresponds to the direction looking straight toward the centre of Venus; the white circle shows the location of Venus' surface. For all three images, the ionopause altitude is 250 km at the subsolar point. In the images from solar zenith angles 100º and 140º, the ENA flux has two local maxima: one on the dayside of Venus and the other in the direction of the Sun. The latter maximum is produced upstream of the bow shock by charge exchange collisions between the protons in the unperturbed solar wind and atoms in the

Table 1. A comparison of some aspects of the ENA simulations for Venus and Mars.

	Venus ionopause 250 km	*Venus ionopause 400 km*	*Mars (empirical; Holmstrom)*	*Mars (MHD; Gunell)*	*Unit*
ENA production rate	7.8×10^{24}	5.6×10^{24}	1.7×10^{25}	2.4×10^{25} min 5.1×10^{24} max	s^{-1}
ENA escape rate	5.3×10^{24}	4.0×10^{24}	1.5×10^{25}		s^{-1}
ENA precipitation rate	2.2×10^{24}	1.2×10^{24}	1.4×10^{24}		s^{-1}
ENA max. flux	5.8×10^{10}	3.8×10^{10}	3.0×10^{11}	1.1×10^{11}	$sr^{-1}\ m^{-2}\ s^{-1}$

Values for Venus are given for ionopause altitudes 250 km and 400 km. Venus' upper atmosphere is approximately independent of the solar cycle. The values for Mars from Holmstrom et al. (2002) are all for solar minimum conditions. Values from the MHD simulation of Mars were taken from Gunell et al. (2005b). 'Max. flux' refers to the maximum flux in an ENA image of the interaction region downstream of the bow shock. Solar minimum and maximum conditions are denoted by 'min' and 'max', respectively.

exosphere of Venus. At 180º the Sun is occulted by Venus. The ENA production, escape and precipitation rates were calculated for ionopause altitudes of 250 km and 400 km. These numbers, together with the corresponding numbers for Mars, are found in Table 1. For Mars, both the numbers obtained by Holmström et al. (2002) using an empirical plasma flow model and those obtained by Gunell et al. (2005a) using an MHD model are reported.

The precipitation rate at Venus is higher than at Mars. This is not unexpected because Venus is a larger planet, and the ENA production region is closer in than at Mars, which is seen in Fig. 6. The left panel of Fig. 6 shows an ENA image of Mars (Gunell et al., 2005a), based on an MHD model for the plasma flow (Ma et al., 2002). The right panel shows an ENA image of Venus.

The ENA flux and production rates at Venus are lower than at Mars even though the solar wind flux is more intense at Venus. The reason for this is that the neutral gas density at relevant heights is lower in Venus' than Mars' exosphere. The neutral density falls off more rapidly with altitude at Venus, because of the larger mass of that planet, which is 7.5 times greater than the mass of Mars. The dominant contribution to the neutral density at high altitudes at Mars during solar minimum conditions is the large hydrogen corona (Krasnopolsky & Gladstone, 1996). The hydrogen density at Mars is greater than that at Venus everywhere above the exobase, and hydrogen is by far the most important species for ENA production at Mars (Holmström et al., 2002).

To show the contributions from different regions, and to illustrate the differences between Venus and Mars, the contributions from different positions along a line-of-sight are examined. Fig. 7 shows, in the three panels on the left side, from top to bottom, the total neutral gas density, the plasma flux, and the rate of ENA production in the direction toward the vantage point, as functions of distance along the line of sight from the vantage point. The ENA production rate, when integrated along the line of sight, gives the differential ENA flux that is shown in the ENA images. The right panel shows the lines-of-sight along for which the different quantities are plotted in the left panels. The filled red circle represents Mars and the yellow Venus. The vantage points are at solar zenith angle 100° and a planetocentric distance of three radii of the respective planet. The direction of the lines of sight corresponds to the direction of the pixel with the maximum flux of an ENA image from that vantage point. Because the topology of the plasma flow is different at Venus and Mars the directions of the maximum flux is also different at the two planets. The higher exospheric density at Mars is what makes the ENA flux at Mars greater than at Venus, as is seen in the top left panel. Although the solar wind density is higher at Venus, the flux in the relevant region, i.e., close to the planet, is similar to that at Mars (middle left

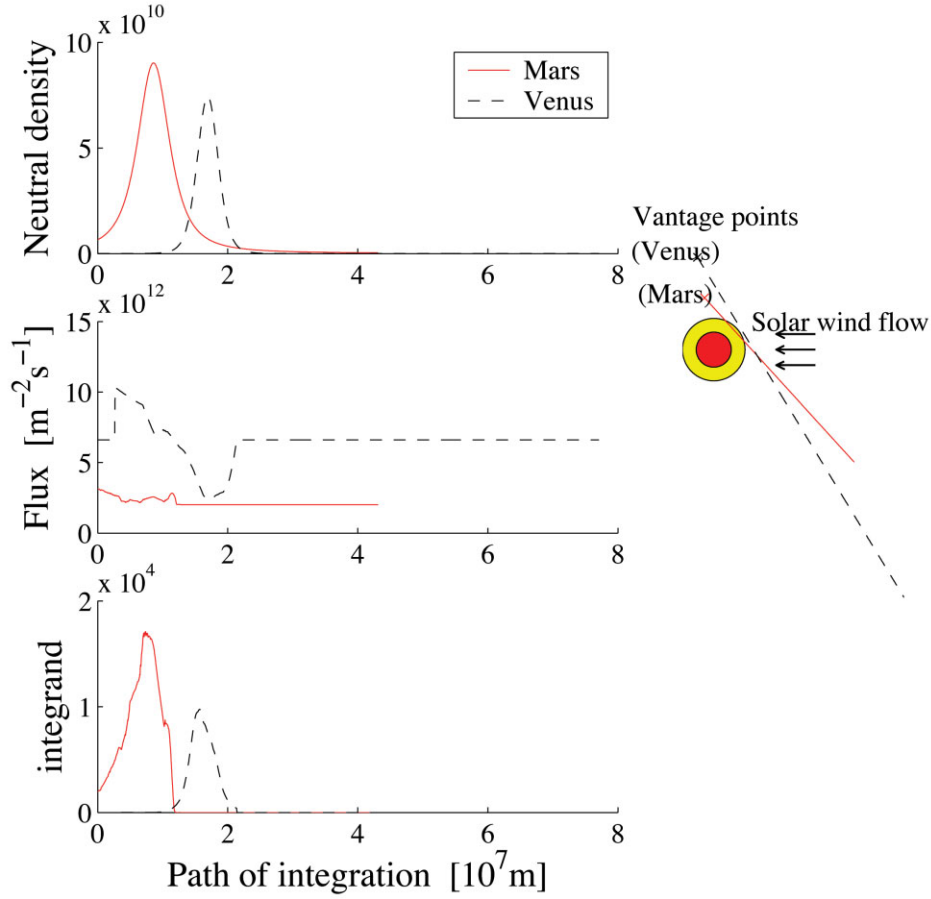

Fig. 7. The panels on the left side show, from the top, the total neutral gas density, the plasma flux, and the rate of ENA production in the direction toward the vantage point, as functions of distance along the line-of-sight from the vantage point. Solid and dashed lines represent values at Mars and Venus, respectively. The right panel shows the lines-of-sight for which the different quantities are plotted at left. The red circle represents Mars and the yellow Venus.

panel). The bulk speed of the plasma is slowed near the planet, and the line-of-sight that yields the highest differential flux is farther from the planet at Mars than at Venus.

It is interesting to compare the results obtained here with those of Fok et al. (2004). Although their parameters are not identical, they are similar. Fok et al. (2004) took the effect of spacecraft motion into account; we do not. Since we are considering ENAs with energies above 50 eV, this amounts only to a small correction in this case. Both models yield ENA fluxes of the same order of magnitude and one can conclude that they are in reasonable agreement considering their uncertainties. Real measurements are required to determine between them, or indeed to say anything conclusively about the accuracy of the models.

2. The Instrument

2.1 Overall configuration

The ASPERA-4 instrument is a replica of ASPERA-3 on Mars Express (Barabash et al., 2004). It is a comprehensive plasma diagnostic package to measure ENAs, electrons and ions with a wide angular coverage from a 3-axis stabilised platform. Mechanically ASPERA-4 consists of two units, the Main Unit (MU) and IMA (Fig. 8). The MU has three sensors: NPI, NPD and ELS, plus a digital processing unit (DPU), on a turnable platform. The combination of the 360° sensor field-of-view (FOV; 180° for NPD) and the scans from 0° to 180° give, ideally, the required 4π maximum coverage, but part of the FOV is blocked by the spacecraft body. The actual coverage depends on the sensor location on the spacecraft. All electrical interfaces with the spacecraft are made

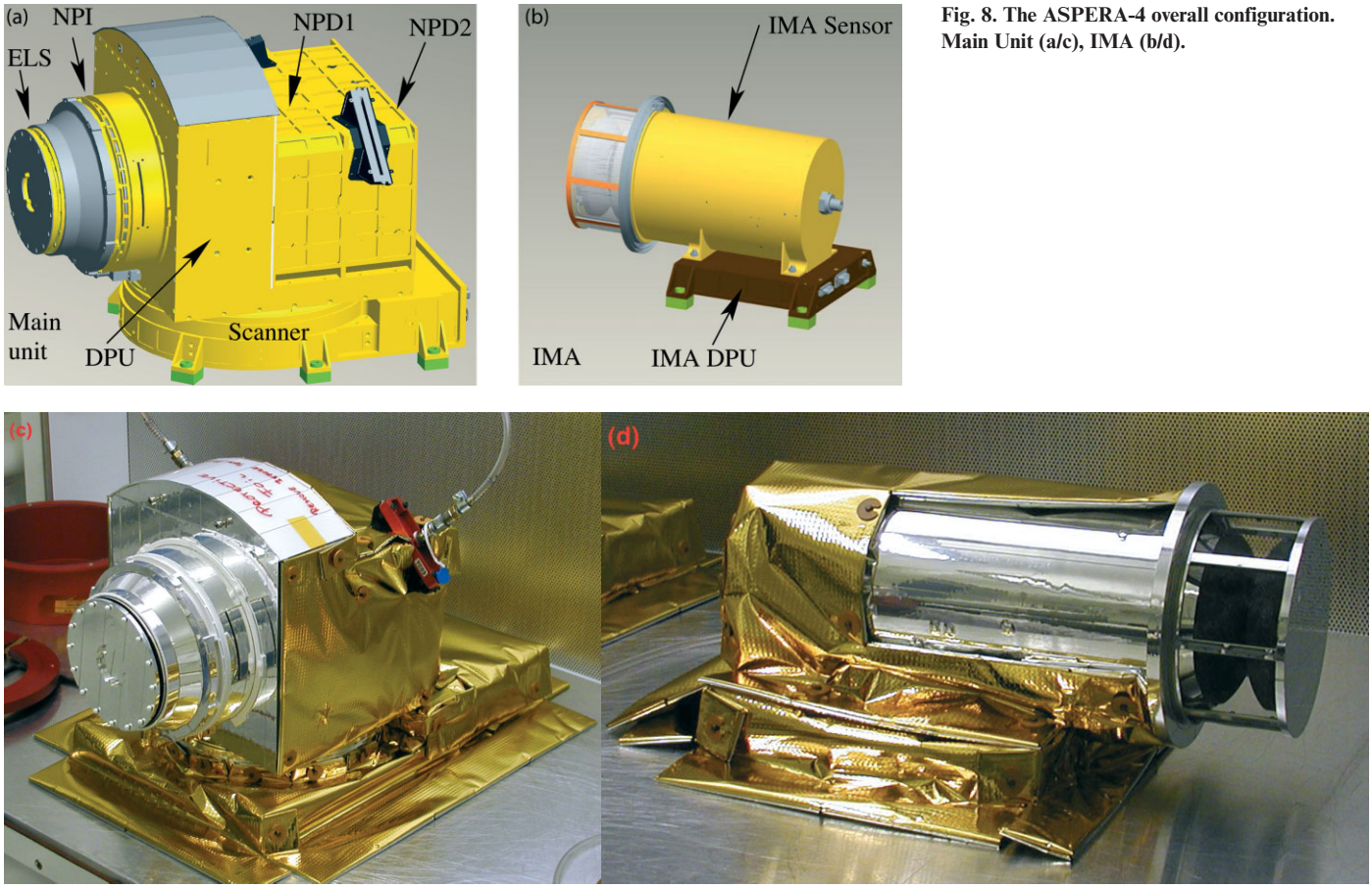

Fig. 8. The ASPERA-4 overall configuration. Main Unit (a/c), IMA (b/d).

through the scanner. Electrically, IMA interfaces only to MU. The total mass of the instrument is 9.00 kg. The MU mass without thermal hardware is 6.63 kg; the IMA is 2.37 kg without thermal hardware. The maximum power consumption is 18 W. The MU envelope is 350 x 263 x 288 mm; for IMA it is 287 x 187 x 165 mm.

The two ENA sensors are complementary. NPI provides measurements with relatively high angular resolution but no mass and energy discrimination, while NPD performs mass and energy analysis of the incoming ENAs, but the angular resolution is crude. This approach provides the necessary redundancy and the independent cross-checking that is necessary for such measurements in a new environment. The charged particle sensors not only characterise the local plasma environment but also support ENA measurements with charged-particle background measurements and inter-calibrations.

ELS is a standard top-hat electrostatic analyser of a very compact design and with high energy resolution. IMA is an improved version of the ion mass spectrographs TICS/Freja, IMIS/Mars-96, IMI/Planet-B (Norberg et al., 1998), and a copy of the Ion Composition Analyser (ICA) flying on the Rosetta mission. Since IMA is not accommodated on the scanner, electrostatic sweeping is used to achieve the ±45° elevation coverage.

The instrument design, while based on a modular structure, has a high degree of packaging and sharing of internal resources. The DC/DC converters are shared between all five units, including the two identical NPD sensors. The DPU mechanical structure also serves as the carrying support for mounting the NPD sensors and NPI which, in turn, carries the ELS. The internal walls that separate the DPU, NPI and the two NPD sensors were replaced by conductive Kapton

Table 2. Baseline performances of the NPI, NPD, ELS and IMA sensors.

Parameter	*NPI*	*NPD*	*ELS*	*IMA*
Particles to be measured	ENA	ENA	electrons	ions
Energy range, keV per charge	≈ 0.1–60	0.1–10	0.01–20	0.01–36
Energy resolution, $\Delta E/E$	No	0.5	0.08	0.07
Mass resolution	No	H, O	–	m/q = 1, 2, 4, 8, 16, 32, >40
Intrinsic field of view	9° x 344°	9° x 180°	4° x 360°	90° x 360°
Angular resolution (FWHM)	4.6° x 11.5°	5° x 30°	2° x 22.5°	4.5° x 22.5°
G-factor*/ pixel, cm^2 sr	2.7×10^{-3} (ε not incl.)	6.2×10^{-3} (ε not incl.)	7×10^{-5}	3.5×10^{-4}
Efficiency, ε, %	~ 1	0.5–15	inc. in G	inc. in G
Time resolution (full 3D), s	32	32	32	196
Mass, kg	0.7	0.65 each	0.3	2.2

*G-factor is the instrument geometrical factor

foils to minimise mass, while maintaining sufficient electromagnetic shielding. Tantalum point shielding is used because of the high radiation hardness requirement (30 krad). ELS uses an external metallic conical ring to protect the sensitive electronics. Table 2 summarises the instrument performance.

2.2 The Neutral Particle Imager

The Venus Express NPI is a spare model of the ASPERA-3 NPI from Mars Express which, in turn, is a replica of the NPI-MCP sensor developed for the ASPERA-C instrument on Mars-96 (launch failure) and successfully flown on the Swedish Astrid microsatellite, launched in 1995 (Barabash, 1995).

The charged particles, electrons and ions are removed by the electrostatic deflection system, which consists of two discs separated by a 3 mm gap (Fig. 9). The 5 kV potential between the grounded and biased discs results in a strong electric field, which sweeps away all charged particles with energies up to 60 keV. Since the integral ENA flux substantially exceeds the charged particle flux for energies greater than 60 keV, this rejection energy is sufficient. The discs also collimate the incoming beam over the azimuth angle. Apart from being ON or OFF, the deflection system can be operated in two other modes: alternative and sweeping. In the alternative mode, the deflection system is turned on and off for one sampling time. This is used for more accurate separation between charged and neutral particles entering the system. The deflection system is connected to the high-voltage supply via an optocoupler. Regulating the optocoupler reference voltage changes the deflection voltage performing the sweeping and alternating. In order to reduce the time for discharging the deflection system discs to 1 ms, a second parallel optocoupler is used.

The space between the deflection system discs is divided into 32 sectors by plastic (PEEK) spokes forming 32 azimuthal collimators with a FOV of 9º x 18º each. Neutrals passing through the deflection system hit a 32-sided cone target at a grazing angle of incidence of 20º. On impact, the incident neutral can either be reflected, produce secondary particles, or both. The secondaries are both ions and electrons. A 56 mm-diameter PHOTONIS micro-channel plate (MCP) stack in a chevron configuration followed by a 32-sector anode detects the particles leaving the target. The signal from the MCP gives the direction of the primary incoming neutral. The MCP operates in ion mode with a negative bias of slightly more than –2.2 kV applied to the front side and thus detects sputtered positive

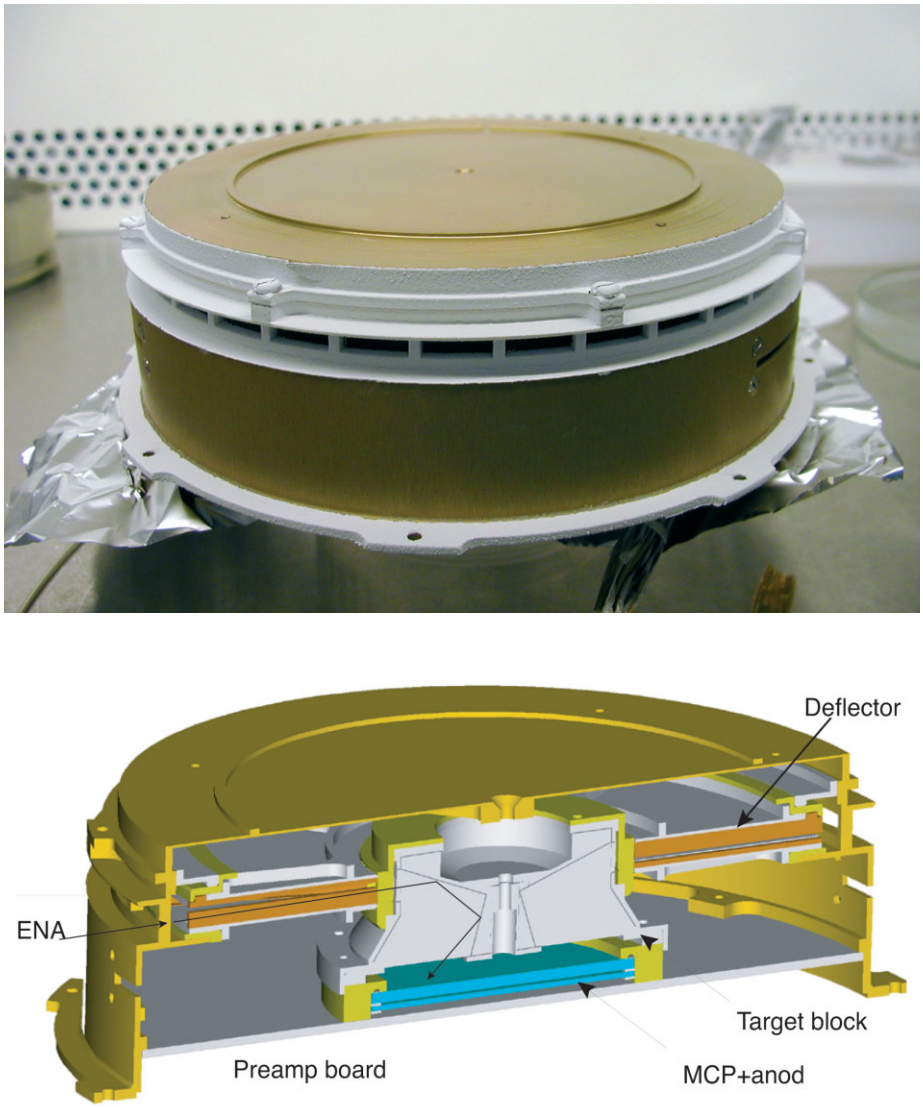

Fig. 9. The NPI sensor.

ions of the target material, positive ions resulting from ionising of the primary neutrals, and neutrals reflected from the target surface. In order to improve the angular resolution and collimate the particles leaving the interaction surface, separating walls are attached to the target, forming a star-like structure. This configuration allows the entering particles to experience multiple reflections and reach the MCP. NPI covers 4π in one scanner scan (except a fraction blocked by the spacecraft body) and produces an image of the ENA flux distribution in the form of an azimuth x elevation matrix. The direction vector of 32 elements is read out once every 62.5 ms. Two sectors centred around the spin axis and looking toward the spacecraft body are blocked intentionally to provide monitoring of the MCP assembly dark counts. This space is also used for the ELS sensor harness. Fig. 10 provides internal views of the NPI sensor.

Calibration was performed to characterise the sensor response, including MCP saturation bias, dark count level, angular response in elevation and azimuth, and efficiency. One sector (number 4) was thoroughly investigated, and a scan with the calibration beam in the central plane of all sectors was used to find the relative response of the other 31 sectors. The calibration was performed using an ion beam as the particle source. This is equivalent to using an ENA

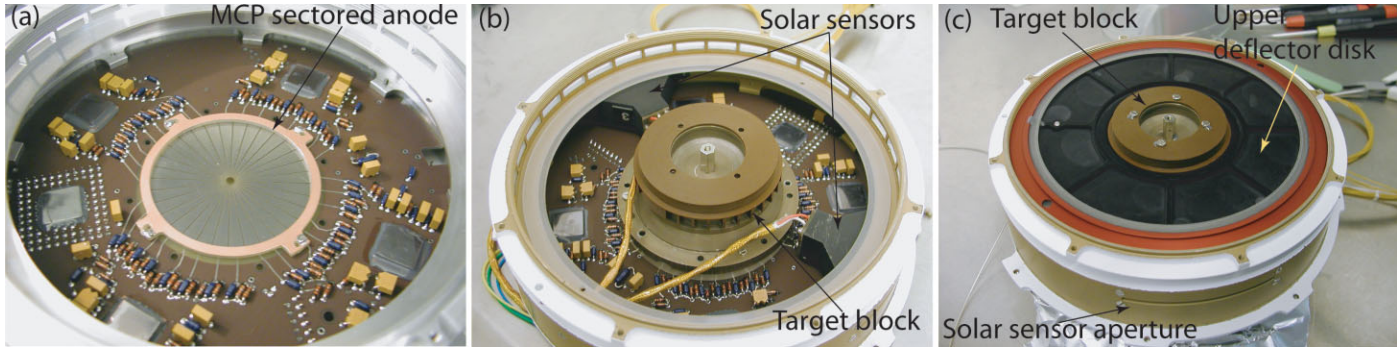

Fig. 10. NPI components: the sectored anode (a), the target block installed (b) and the deflection system installed (c).

beam, since particles 'forget' their initial charge state when interacting with the surface of the target block.

Fig. 11 shows the efficiency of the NPI measured with H_2O^+ ions and protons in the beam for different MCP bias and energies. The efficiency was measured in sector 4 with the neighbouring sectors mechanically blocked. For the MCP operating bias of –2.2 kV, the efficiency for solar wind energies (~ 1 kV) is around 5 x 10^{-4}. Fig. 12 shows a scan in the central plane of all sectors over a wide parallel beam of 5 keV protons. This measurement was performed to calibrate the relative sensitivity of the sectors, which varies significantly. Since the sector angular (polar-azimuth) response function should be included in the ENA image inversion models, it was measured and analytical fits were produced. The upper panels of Fig. 13 show the measured data and response function; the lower panels show a polynomial fit to the response.

An important design issue was the coating of the target block for suppressing UV photon fluxes, which enter the instrument and produce the UV background in the measurements. NPI uses the same coating as in the experiments Prelude in Planetary Particle Imaging (PIPPI) on Astrid-1 and ASPERA-C on Mars-96: DAG 213, a resin-based graphite. The PIPPI coating gave satisfactory performance in the Earth's magnetosphere (C:son Brandt et al., 2000). To determine the target-block UV separation, NPI was calibrated against hydrogen Lyman-alpha photons (121.6 nm). The calibration philosophy was similar to

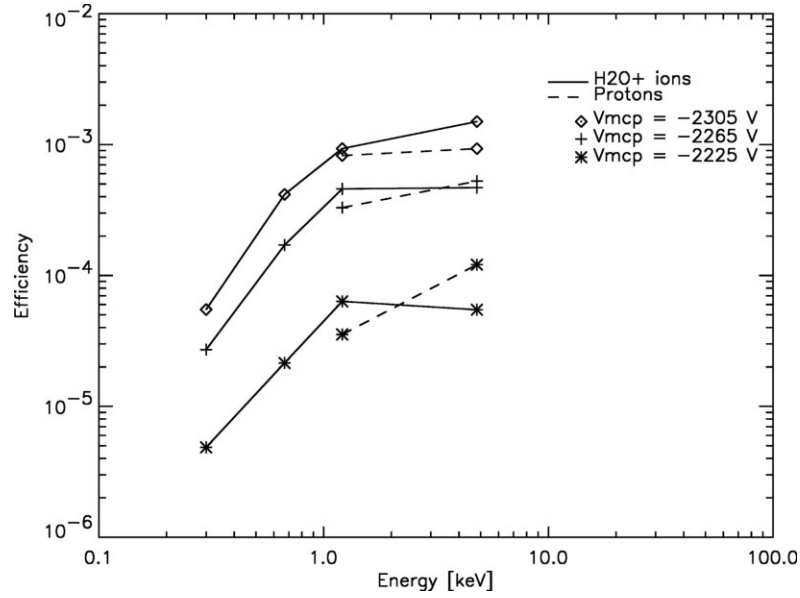

Fig. 11. The efficiency of sector 4 with neighbouring sectors mechanically blocked.

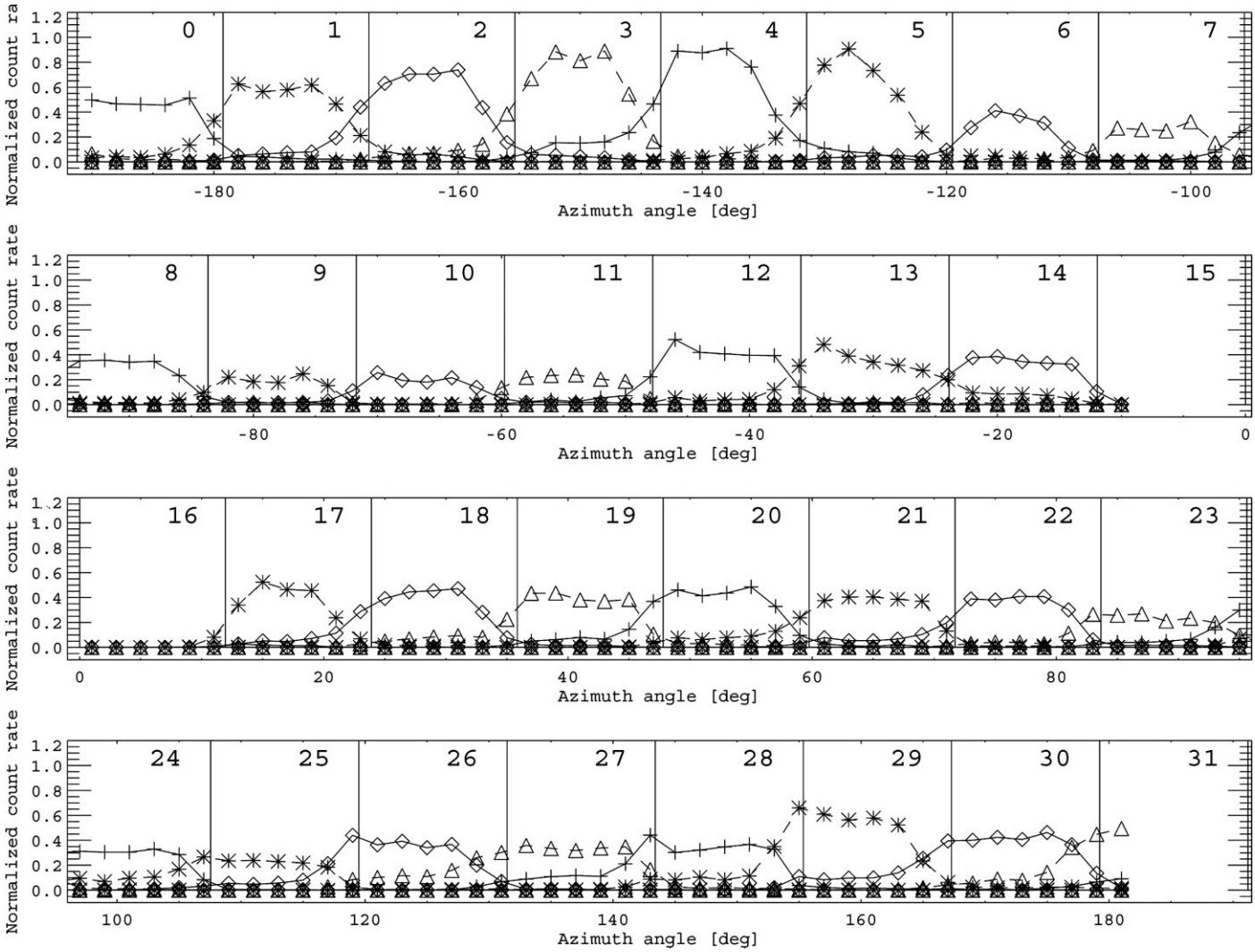

Fig. 12. Scan through the central plane of the sectors.

that of the particle calibration in that the response of one sector (number 4) was fully characterised then a relative measurement was made for the other sectors.

During the calibration at the University of Arizona, the UV intensity in the beam was continuously monitored by an absolutely calibrated channeltron. The maximum intensity measured was 10^7 photon/s into the NPI aperture. The measured count rate was ~30/s, which corresponds to a UV suppression efficiency of $10^7/30 \sim 3 \times 10^5$. This is somewhat higher than previously reported by Barabash (1995).

The intensity measurement is important for understanding the NPI UV response. Knowing that the response is more or less linear within certain intensities, we can scale the response against the space level to determine the photon-related background. Owing to an unstable beam, only three points on this curve were obtained. The NPI count rates for the respective UV (Lyman-alpha) beam intensities are plotted in Fig. 14.

The relative response of other sectors against the Lyman-alpha was measured with the beam centred in the aperture of each sector. The sensor response against normalised beam intensity is shown in Fig. 15.

Fig. 16 shows an example of NPI data from ASPERA-3 on Mars Express. Simulations of the ENA emissions from the corresponding directions (sectors) are included. The increase in the count at around 20:10–20:20 UT results from

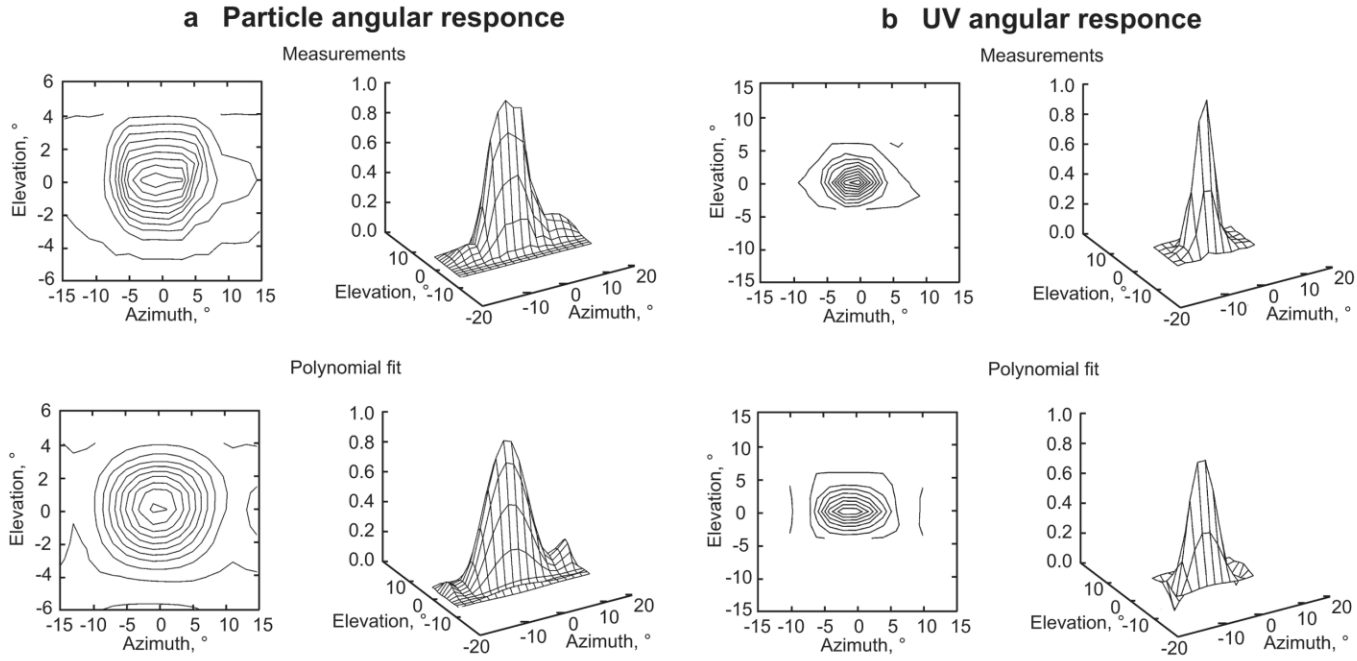

Fig. 13. Left: full angular scan with sector 4 in the particle beam (protons). The lower panels show a polynomial fit. Right: full angular scan with sector 4 in a UV photon beam (Lyman-alpha). The lower panels show a polynomial fit.

ENA fluxes generated in the Martian magnetosheath when the shocked solar wind protons charge exchange on the exosphere and move further as hydrogen atoms along lines tangential to the solar wind stream lines. Important parameters can be found from data such as the position of the Induced Magnetosphere Boundary near Mars (Gunell et al., 2006).

2.3 The Neutral Particle Detector

The NPD sensor consists of two identical detectors, each a pinhole camera. Fig. 17 provides a conceptual view of one detector. In each, the electrons and ions are removed by a deflection system, which consists of two 90º sectors separated by a 4.5 mm gap. In the normal operational mode, the 10 kV potential (±5 kV) applied to the discs and the resulting strong electric field sweeps away all charged particles with energies up to 70 keV. The deflector also collimates the incoming beam in the elevation angle. The collimated ENA beam emerging from the 3.5 x 4.5 mm pinhole hits the START surface under a 15º grazing angle, causing secondary electron emission. By a system of collecting grids, the secondary electrons are transported to one of two MCP assemblies that give the START signal for the time-of-flight (TOF) electronics.

Depending on the azimuth angle, the collection efficiency varies from 80% to 95%. The incident ENAs are reflected from the START surface near-specularly. Since the charge-state equilibrium is established during the interaction with the surface, the emerging beam contains both the neutral and ionised (positive and negative) components. To increase the total efficiency, no further separation by the charge is made.

As proved by the ion tracing, there is very little disturbance to the reflected atomic ions leaving the START surface with an energy above 80 eV, introduced by the START electron optics. Fig. 18 shows the results of electron and ion ray-tracing in the START assembly electron optics.

Particles of all charge states thus impact the second (STOP) surface, and again produce secondary electrons, which are detected by one of the three MCP assemblies, giving the STOP signal. The TOF over a fixed distance of 8 cm defines the particle speed. Three STOP MCPs also give crude resolution over azimuth within a 90º acceptance angle. Since the secondary electron yield

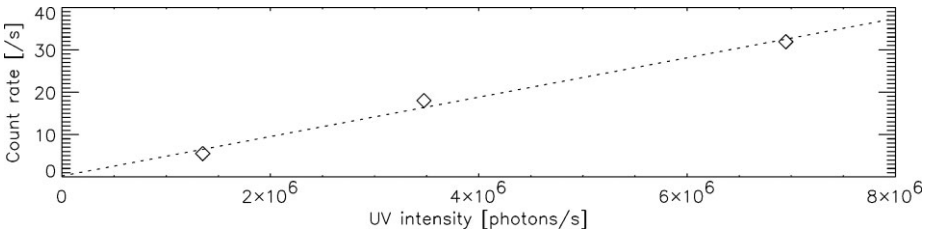

Fig. 14. NPI sensitivity to UV intensity.

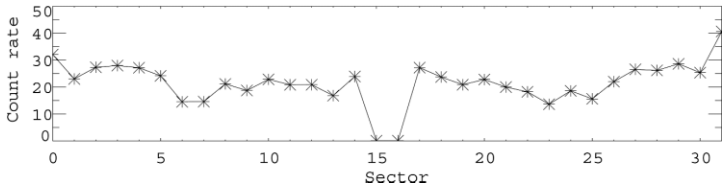

Fig. 15. The relative response of all sectors to the UV photons (Lyman-alpha). The measurements are taken with the UV beam centred on the aperture of each sector. Count rate in count/s.

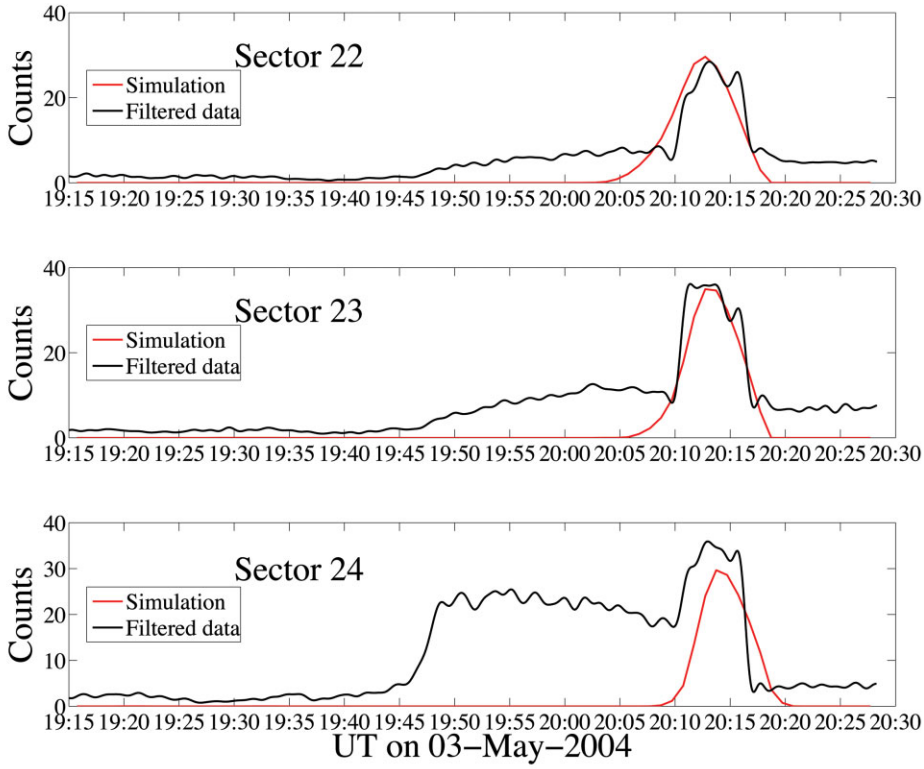

Fig. 16. Simulations (red curves) and filtered data (black curves) from Mars Express orbit 363 and the ASPERA-3 NPI sensor. The highest count rates in sector 23 correspond to a flux of 1.3 x 10^{11} m^{-2} sr^{-1} s^{-1}.¶

depends on mass for the same speed, the pulse height distribution analysis of the STOP signals provides the estimate of ENA mass. Each event is stored in the array STOP MCP charge x TOF x direction. The array is accumulated over the sampling time 62.5 μs.

Fig. 19 shows the NPD flight model. Two identical sensors are in a package on the scanning platform, providing a 180° scan for 2π coverage.

The selection of the START and STOP surfaces was the most challenging part of the development. Extensive studies were performed at University of Bern (Jans, 2000) and Brigham Young University (USA) to optimise the performance of the surfaces which must satisfy a number of requirements: high secondary electron yield, high UV absorption even at grazing angles, high particle reflection

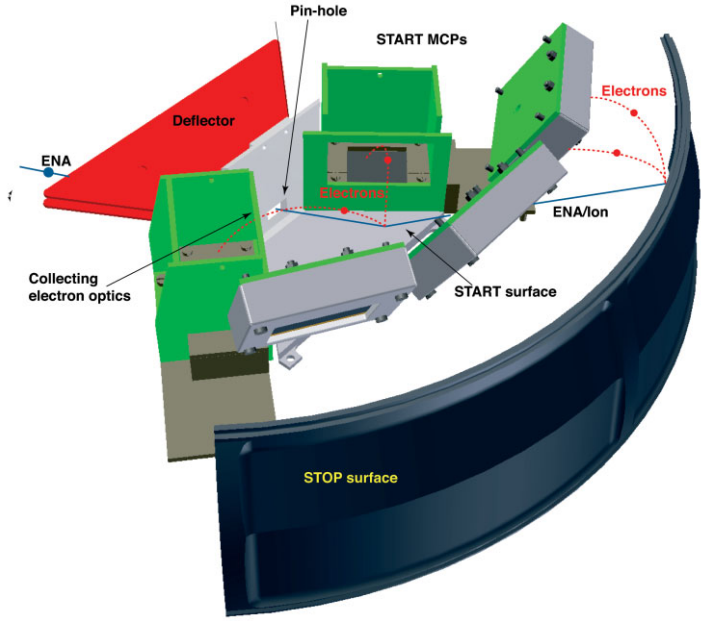

Fig. 17. The principal components of NPD .

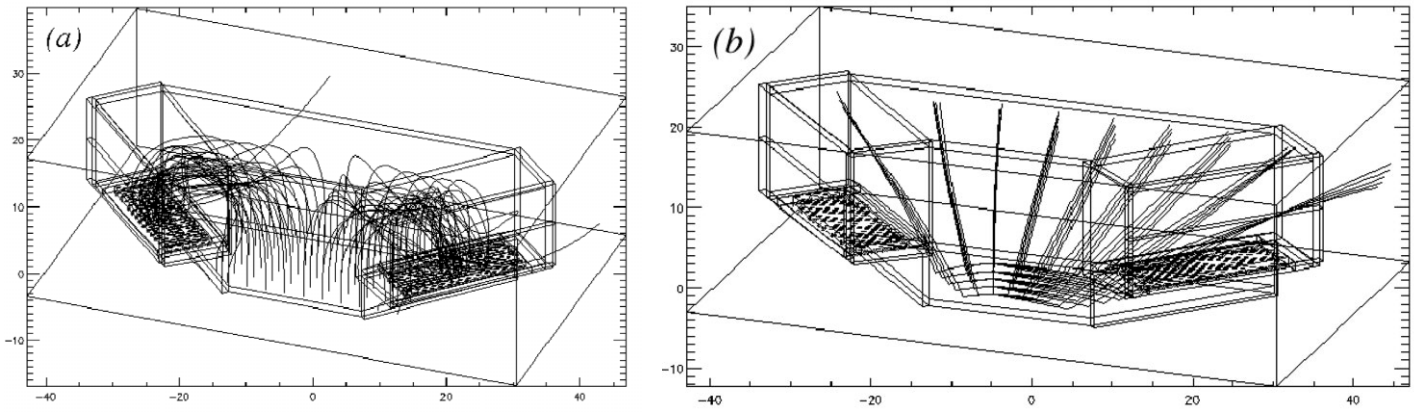

Fig. 18. Ray-tracing of electron (a) and 80 eV ion trajectories (b) in the START assembly optics.

coefficient (START surface), low angular scattering, and low photoelectron yield. For the START surface, a multi-layer coating of a thin layer of Cr_2O_3 was chosen, covered by a thicker layer of MgF, topped with a thin layer of WO_2. The coating is optimised for the absorption of the 121.4 nm line at the 15° incidence angle. The reflection coefficient reached was about 30%, a factor of 2 lower than the uncoated surface. The coating was applied on a titanium substrate polished down to 100 Å roughness.

The STOP surface is graphite (roughness around 100 nm) covered by an MgO layer of about 500 nm. This combination has a very high secondary electron yield, low photoelectron yield and high UV absorption. A great effort was made to increase the stability of the MgO coating against moisture. It was established that polishing the graphite substantially improves the stability against possible rises in air humidity during storage and pre-launch operations, but does not present any problems for the surface performance. Therefore, both surfaces were stable and did not require special maintenance.

The NPD calibrations included determining the efficiency, geometrical factor, angular response and energy resolution. The results fully correspond to the specified performance. Since charge-equilibrium establishes over just a few Å at the particle-surface interaction, ion beams can be used for calibrations of ENA

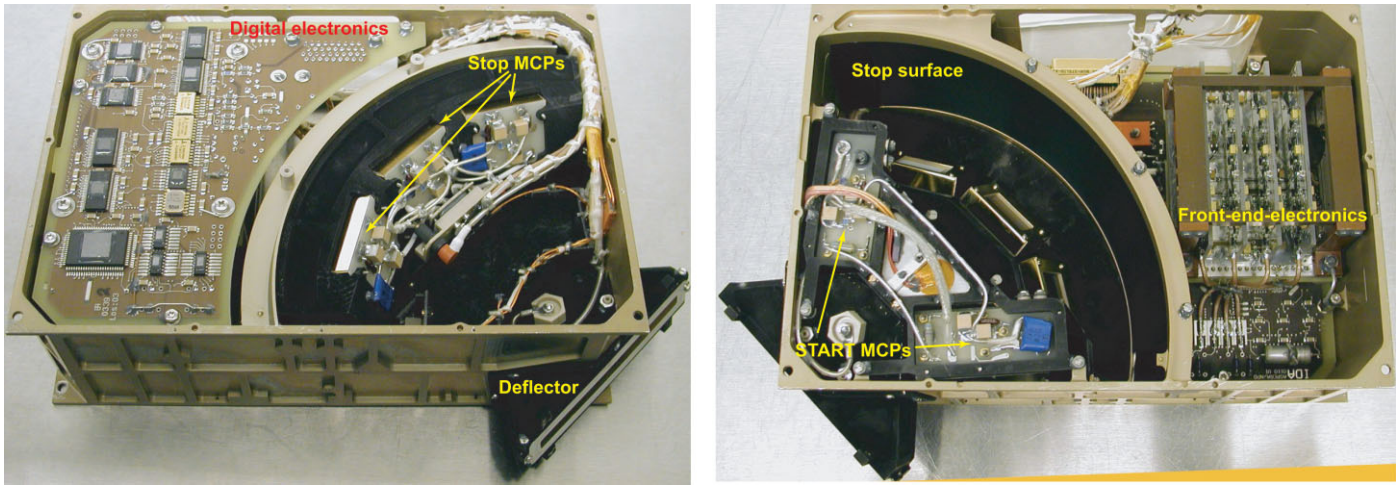

Fig. 19. Top and bottom views of the NPD flight model.

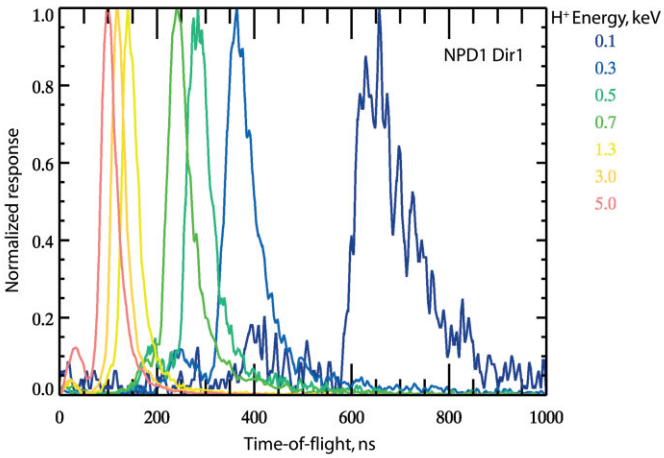

Fig. 20. NPD TOF spectra of proton beams at different energies.

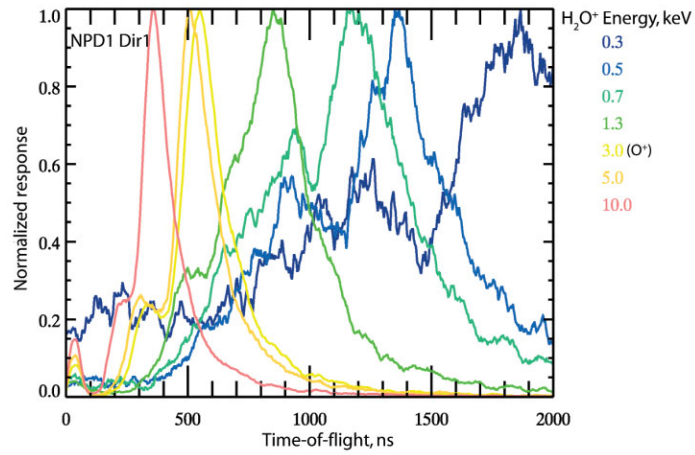

Fig. 21. NPD TOF spectra of H_2O beams at different energies.

sensors. Fig. 20 shows the TOF distributions for a proton beam at different energies (colour-coded) in the energy range 0.1–5.0 keV. The displacement of the peaks from the exact energy of the incident particles reflects the energy loss of 33%, which is independent of energy. The full width at half maximum (FWHM) is about 80%. Fig. 21 shows the TOF distributions for H_2O^+ ion beams of different energies covering the energy range 0.3–10.0 keV. The energy losses are the same as for the proton beams.

Fig. 22 shows the calibrated dependence of the measured TOF on the incoming particle energy for protons and H_2O^+ ions. The dashed lines show the theoretical dependence corresponding to the 33% energy loss in the START surface. The water molecules produced in the ion source break up during the impact, but the residual components carry the same initial velocity corrected for the energy loss in the target. Therefore, water can be used to calibrate the response of the instrument to oxygen beams. Since the TOF for oxygen with an energy below 2 keV is longer than the TOF corresponding to slowest protons at around 100 eV, TOF measurements alone can be used to identify the particle mass at least in the low energy range.

Fig. 23 shows the angular response over azimuth for a 3 keV proton beam for the three STOP sectors. The red line shows the response of the central sector and

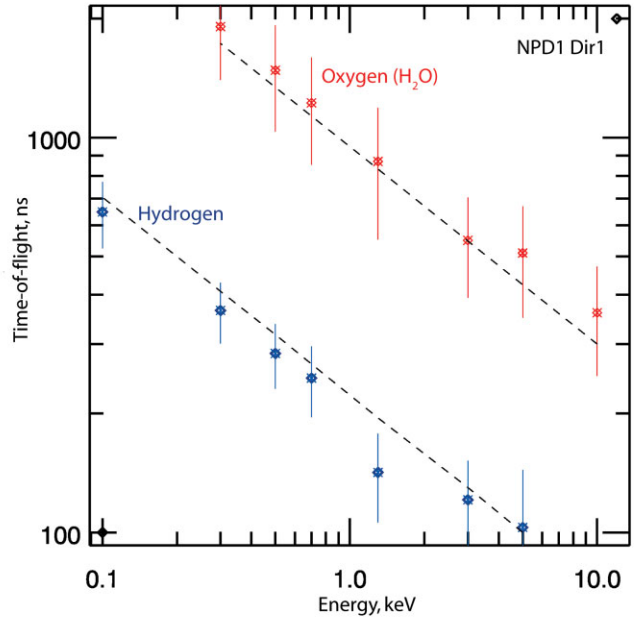

Fig. 22 TOF measurements for different masses as a function of energy. The dashed lines give the theoretical dependence corresponding to 33% energy loss.

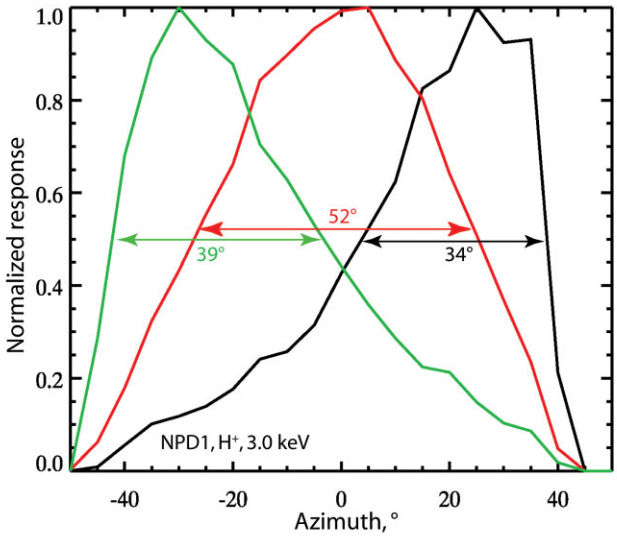

Fig. 23 (below left). The angular response of NPD in the azimuthal direction.

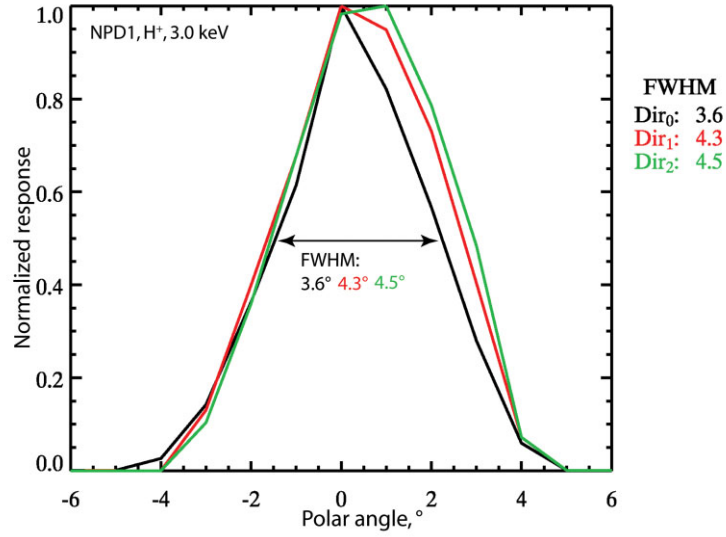

Fig. 24 (below right). The angular response of NPD in the polar direction.

the green and the black lines show the side sectors. Fig. 24 shows the sensor angular response over the polar angle. The FWHM over azimuth varies from 52° for the central sector to 35° and 37° for the two side sectors, respectively. Over polar angle, the FWHM is 4.5° for all directions.

Fig. 25 shows the absolute efficiency of the NPD sensor as a function of energy. The black line corresponds to the incident proton beam, and the grey line to the H_2O^+ beam.

As seen in Fig. 25, the efficiency is more than 11% for H_2O ENAs at 6 keV. For the H ENA, the efficiency reaches 6.5%. Up to a certain energy, the efficiency increases with energy, corresponding to an increase of the secondary electron yield. At the energy where the yield reaches unity, the efficiency levels out (approximately 3 keV for protons and 6 keV for oxygen). At energies below 1 keV, the efficiency is a few percent.

2.4 The Electron Spectrometer

ELS is a new-generation ultra-light, low-power electron sensor (Fig. 26). A

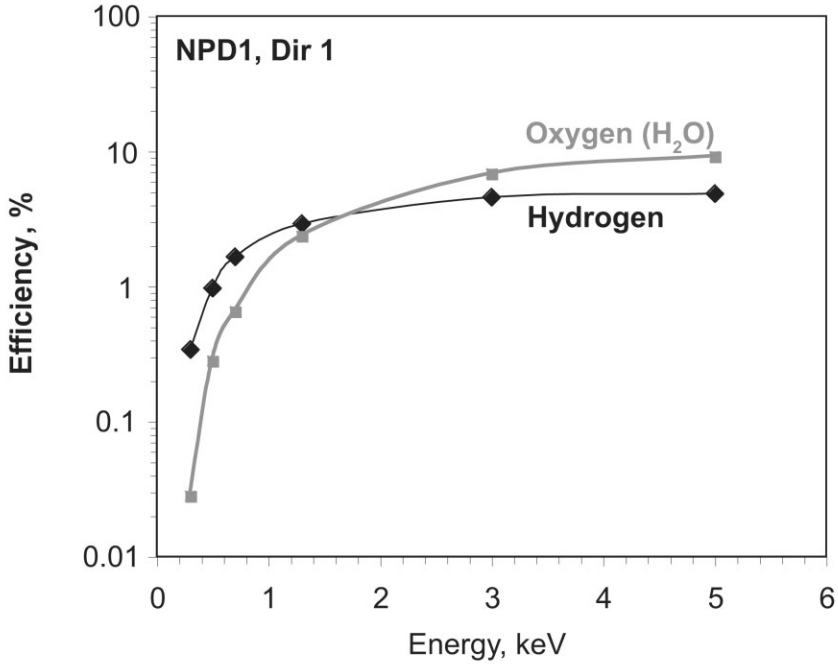

Fig. 25. NPD sensor absolute efficiency.

collimator system is followed by a spherical top-hat electrostatic analyser (Sablik et al., 1990), achieving a geometric factor of 5.88 x 10^{-4} cm^2 sr. The top-hat has a 17° opening angle and a 90° turn angle. The radii of the inner and outer hemispheres are 14.9 mm and 15.9 mm, respectively. Particles enter the aperture at any angle in the plane of incidence. Electrons are then deflected into the spectrometer by applying a positive voltage to the inner hemisphere. The electrons hit an MCP after being filtered in energy by the analyser plates. A spectral measurement is achieved by stepping the plate voltage.

Electrons with energies up to 20 keV/*q* are measured, with a maximum time resolution of one energy sweep (consisting of 128 steps) per 4 s. There are 16 anodes behind the MCP, each anode defining a 22.5° sector and each connected to a preamplifier. ELS is mounted on the ASPERA-4 scanner platform, on top of the NPI sensor, so that the full 4π angular distribution of electrons is measured during each platform scan. Depending on the mode of operation, a sample rotation scan takes 32, 64 or 128 s.

ELS was designed to be solar blind so that it may operate in direct sunlight. This was achieved using two UV-reducing mechanisms and a secondary electron suppression technique. UV is minimised through a series of light baffles in the collimator and a series of UV light traps at the entrance to the spherical deflection plates. Secondary electrons are reduced by a special coating, based on a modified Ebanol-C process, which is included throughout the deflection surface, light trap and collimator system (Johnstone et al., 1997).

There are two small differences between the ASPERA-3 and ASPERA-4 ELS units. One is the inclusion of an outer cylindrical 2 mm-thick aluminium shield, added to prolong operation in the harsher radiation environment of Venus. The other is an offset of the symmetry axes of the deflection plates outside the 1% design specification. The ASPERA-4 ELS, as the refurbished Mars Express flight spare, was built earlier than the ASPERA-3 ELS, and so did not have the advantage of a critical improvement in the fabrication process that ensured the stringent 1% requirement. The misalignment results in differences in instrumental properties as a function of the anode sector position, illustrated in the calibration results discussed below.

ELS was calibrated at the Mullard Space Science Laboratory, University

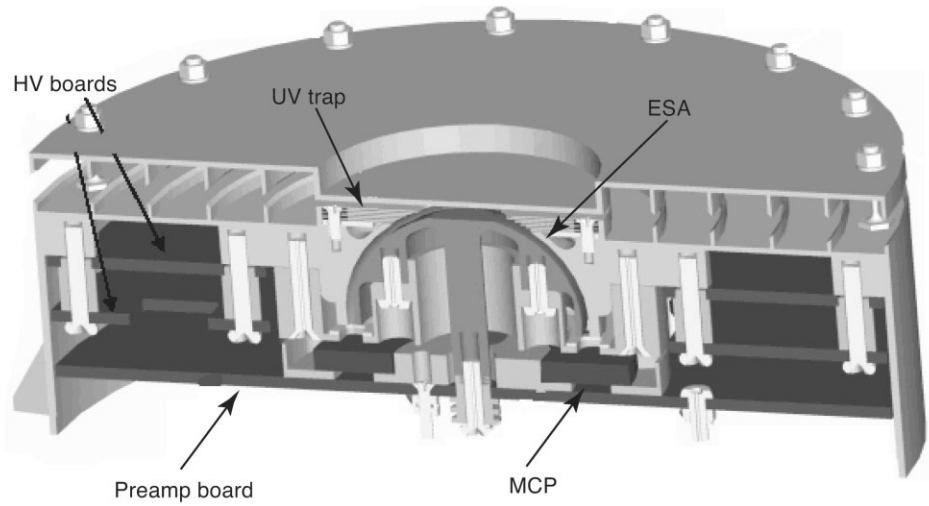

Fig. 26. The ELS sensor.

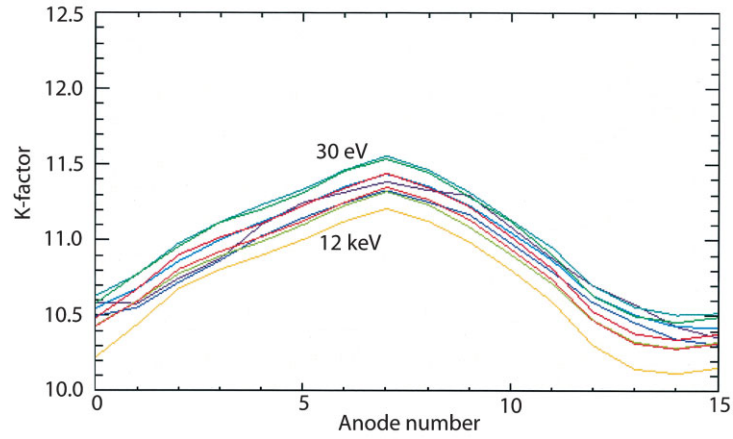

Fig. 27. Plot of the k-factor over 10 energies from 30 eV to 12 keV (violet to red) across the 16 anodes.

College London (UK). The calibration facility (Johnstone et al., 1997), which is based on the technique described by Marshall et al. (1986), provides a wide-area photoelectron beam at energies ranging from a few eV to 15 keV with variable beam intensities from a few Hz to several MHz. The system is fully automated, facilitating calibration scans over the complete range of polar and azimuth angles at several instrument voltage settings for the analyser and the MCP. A flexible data-acquisition system was integrated into the automation to provide simultaneous measurements from the 16 preamplifier channels, coordinated with the instrument position and voltage settings. Before performing the calibration, a profile of the beam output was recorded at each of the calibration energies by a channeltron mounted on an x-y table. The channeltron was mounted as close as possible to the instrument aperture to provide a constant reference to the beam intensity. Owing the mechanical imperfections of the instrument as mentioned above, the laboratory calibrations were critical for defining the instrument response.

The instrument has two operational voltage ranges for the energy sweeps so tests were carried out at several energies in both ranges to cover ±180º in polar and ±3º in elevation. Fig. 27 is a plot of the k-factor across the 16 anodes, giving an average value of 11.33. Although this is higher than the design value of 7.5, owing to the mechanical imperfections, the variation across the anodes is less than 5%, allowing the instrument response to be made good with the calibrations with small errors. The imperfections result in a lower geometric factor but have the advantage of increasing the maximum energy acceptance of the instrument.

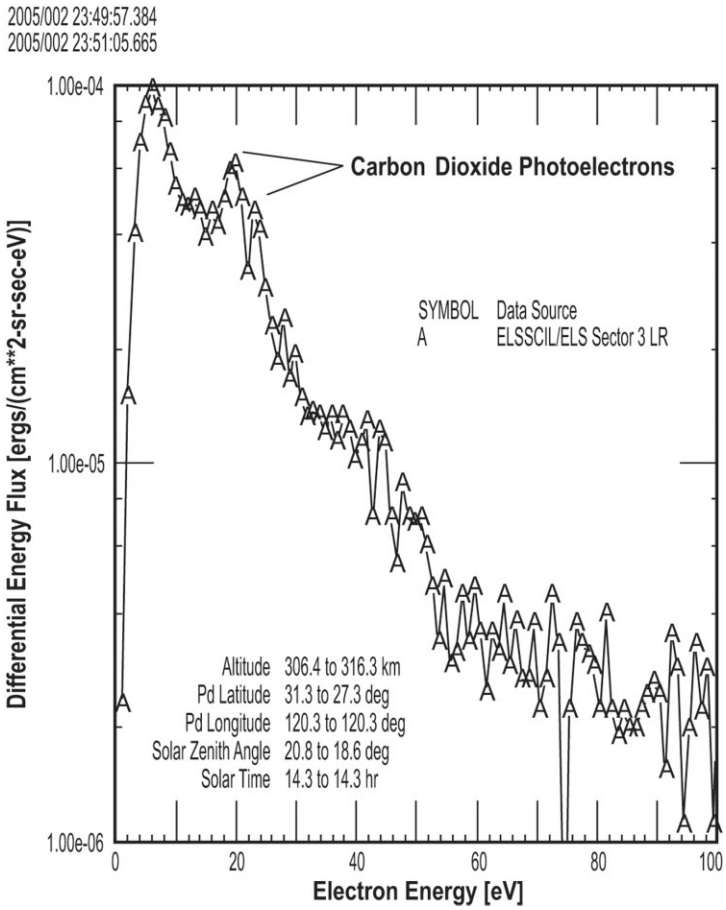

Fig. 28. Photoelectron spectrum from the Martian ionosphere.

The calibrations also established the MCP operational levels for flight and were found to be 150 V higher for ASPERA-4 than ASPERA-3. This is possibly owing to an MCP with a lower intrinsic gain and/or owing to a higher electronics threshold for the readout electronics. Finally, the UV rejection ratio of the analyser was also tested using a Lyman-alpha UV source (Alsop et al., 1996).

ELS has a self-contained, dual-range, linear high-voltage power supply. The first power supply range is from 0 V to about 20 V (about 150 eV) and has 4096 possible settings. The second supply range is from 0 V to 2800 V (about 20 keV) and also has 4096 possible settings. The ELS sweep is fully programmable within the constraint of the maximum decay rate of 32 steps/s. On any given step, the deflection plate voltage is held constant during a minimum of 28.125 ms to accumulate electrons. There is a minimum of 3.125 ms of data latency between energy steps for transition.

In order to obtain high-resolution measurements of the energy spectrum, the power supply may be operated in an oversampling mode, which, when combined with the knowledge of the instrumental response function, increases the number of measurement points per energy interval over a reduced energy range. Measurements in this mode are shown in Fig. 28, which demonstrates a clear resolution of the CO_2 photoelectron peaks, characteristic of the Martian atmosphere.

2.5 The Ion Mass Analyser

IMA (Fig. 29) is an improved version of the ion mass spectrographs TICS (Freja, 1992), IMIS (part of ASPERA-C, Mars-96, 1996) and IMI (Planet-B, 1998) (Norberg et al., 1998). It is a copy of the ICA instrument that is on its way to comet 67P/Churyumov-Gerasimenko aboard Rosetta.

The principal diagram of the instrument is shown in Fig. 30. Ions enter the analyser through the external grounded grid. Behind the grid is a deflection system to vary the incident polar angle of particles (shown in Fig. 30 as trajectories 1, 2 and 3). The deflection angle depends on the voltage applied to the deflector electrodes and lies within the ±45° from the equatorial plane of the instrument. Fig. 31 shows the instrument polar angle response as a function of the deflector voltage. Then ions pass through the top-hat electrostatic analyser, which selects only the given particle energy according to the interplate voltage. Since the top-hat analyser has a full 360° cylindrical symmetry, the azimuthal range (in the plane perpendicular to the symmetry axis) of the instrument is 360°. The parallel incident ion beam is focused in the vicinity of the exit of the top-hat analyser. Thus the particle position at the top-hat analyser exit codes its azimuthal angle. Then the ions pass through the magnetic separation section. The cut of this section in the azimuthal plane is shown in the right panel of Fig. 30. The magnets are shown as blue sectors. Sixteen gaps between the magnets correspond to 16 azimuthal sectors of the instrument of 22.5° each. The radial deviation of the ion trajectories at the exit of the magnetic field region corresponds to particle velocity per charge. Since behind the electrostatic analyser all particles have the same energy per charge value, ion position codes their masses. The particles are registered by an MCP with a position-sensitive anode. The anode resolves 32 bins in the radial position and 16 azimuthal sectors. An example of detector response is shown in Fig. 32.

To measure light ions at low energies, ions such as H^+, which have too small a gyro-radius to reach the MCP, can be accelerated between the top-hat analyser exit and the magnetic section entrance. Fig. 32 shows the 1 keV-particle distribution over the detector surface when the acceleration level is –2150 V. Protons partially reach the MCP for this post-acceleration level. With an acceleration of 3615 V, protons hit the detector at least down to an energy of 300 eV. Fig. 31 shows that the polar angle resolution for constant deflector voltage is about 6°. Fig. 33 shows the azimuthal response of the instrument.

The IMA sensor consists of the ion optics part shown in Fig. 30, a position-

Fig. 29 (below left). The IMA sensor in the vacuum chamber.

Fig. 30 (below right). The analyser (left), with examples of the ion trajectories, and the magnet separator (right).

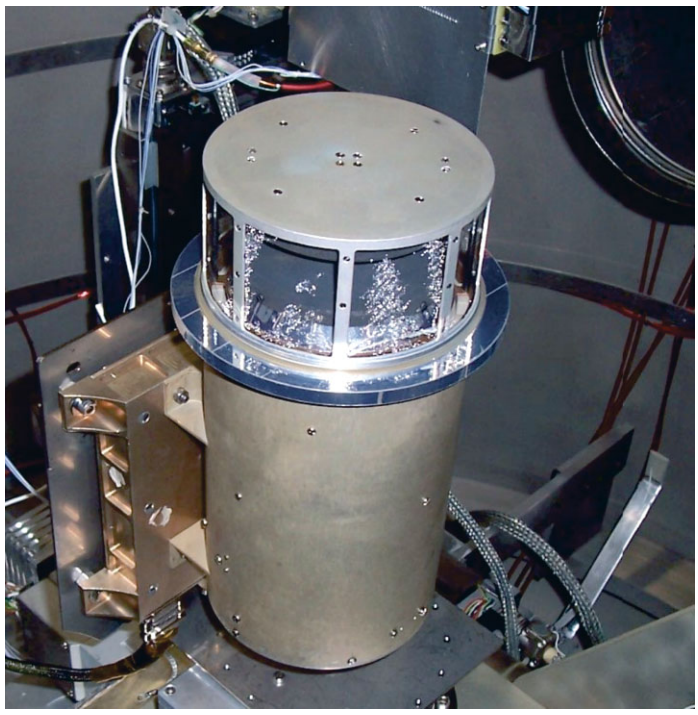

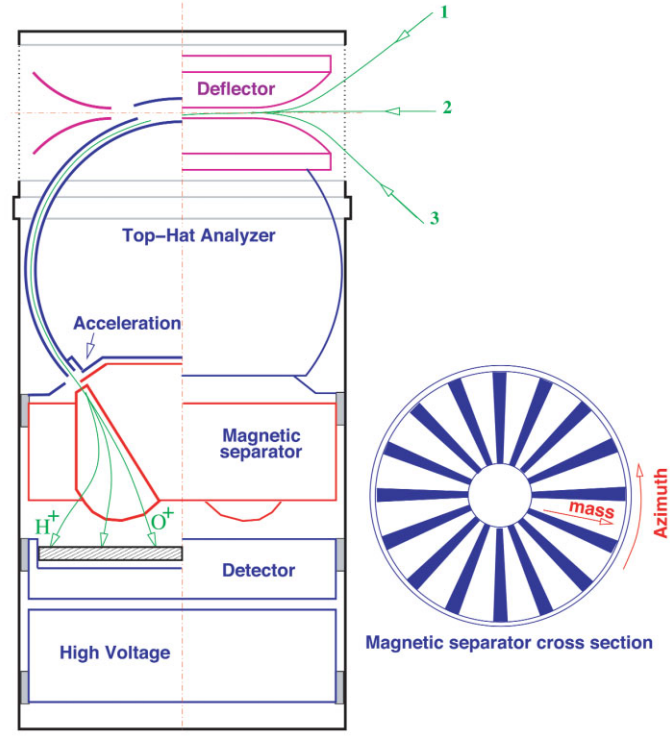

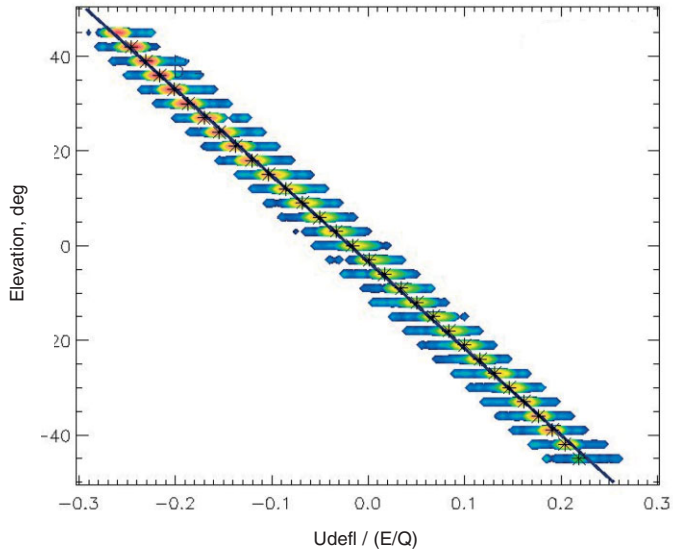

Fig. 31. Colour-coded IMA response as a function of polar (elevation) angle and deflector voltage normalised to the ion energy.

Fig. 32 (below left). Radial profiles of a few mass peaks. The particle energy is 1250 eV, and the post acceleration voltage is –2150 V.

Fig. 33 (below right). Azimuthal response for selected IMA sectors.

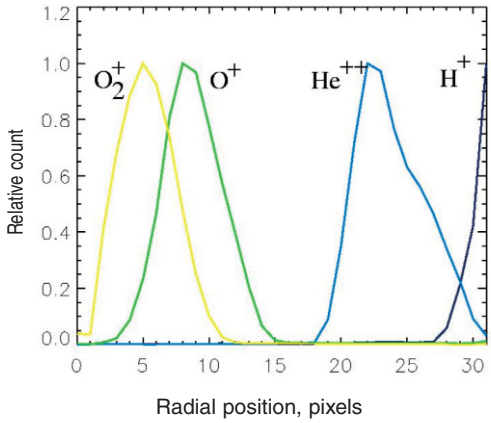

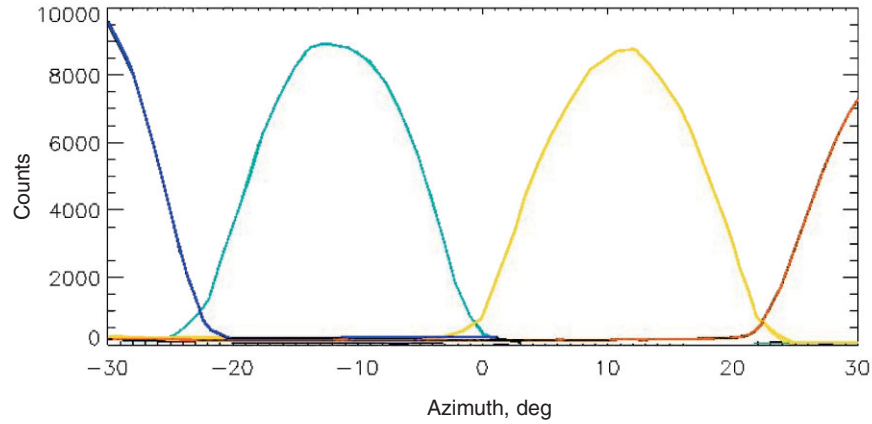

sensitive detector, and a high-voltage unit that provides the sweep voltage for all electrodes and the MCP bias. The sensor is completed by a DPU. Built around a 16-bit MA31750 processor from Dynex, the DPU controls analyser voltages, reads out and accumulates the position information for each detector event, and forms telemetry packets. The hardware operation mode is fixed. The fastest-changing parameter is the particle energy; it sweeps from 30 keV down to 10 eV over 96 logarithmically-equidistant steps. The exposure time on each energy step is 125 ms. During this time interval, 16 radial position spectra (32 points) corresponding to 16 azimuthal sectors are accumulated. After each complete energy sweep, the instrument changes the polar angle of the FOV. The polar angle is scanned from –45° up to +45° over 16 steps. The total time to complete a full 3-D spectrum is 192 s. This spectrum consists of 32 radial (mass) points x 16 azimuthal sectors x 96 energy steps x 16 polar angles.

The data processing involves three stages: logarithmic compression of the count values from 16-bit to 8-bit words; integration (if necessary) over polar angles, and/or azimuthal angles; and RICE compression of the final spectrum. The processing mode is set by telecommand or chosen automatically according to the telemetry rate limitations. The acceleration level is also commandable. Only three values of acceleration are available: 0 V, –2150 V and –3650 V.

Fig. 34 shows an example of an energy-mass matrix obtained by the

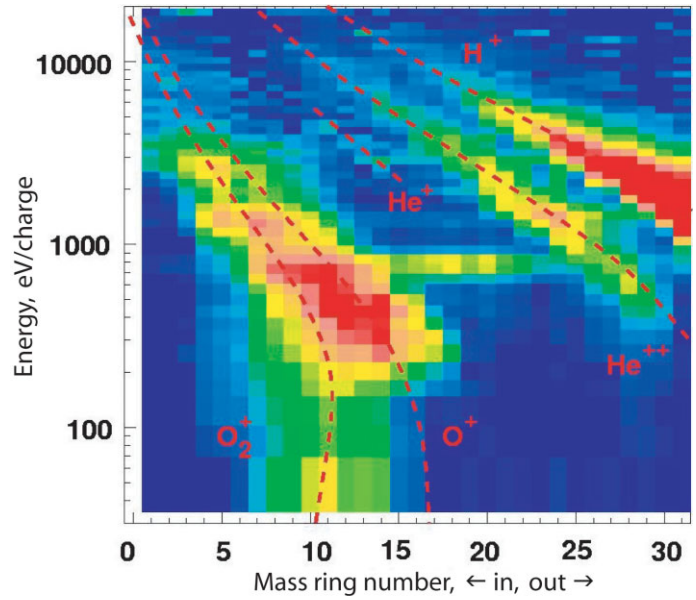

Fig. 34. Energy-mass matrix for post-acceleration voltage of –2000 V, accumulated by the Mars Express IMA sensor for 1.5 years at Mars with the theoretical mass lines. The yellow band at about 700 eV is contamination from the solar wind protons.

ASPERA-3 IMA on Mars Express. The vertical axis represents the energy per charge in eV, and the horizontal axis the sensor's mass ring number. Measurements such as these are used to study the ion composition of the plasma escaping from Mars (Carlsson et al., 2006).

2.6 The Digital Processing Unit

The DPU mechanically has two boards: the DPU board itself (Fig. 35), and a Housekeeping (HK) board (Fig. 36). They are connected through the sensor control electronics and the power supply via a common bus system with 8 address and 16 data lines, besides control, analogue and power supply lines.

The DPU is built around a 16-bit processor MA31750 from Dynex with a 12 MHz system clock frequency and an Actel FPGA RT54SX32S, which implements memory management, watchdog functions and the serial spacecraft interface protocol. The software runs inside a 128 kByte RAM organised in two banks of two 32 kByte static memory chips each. On power-up, a 2x 16 kByte bipolar PROM (Harris) is activated with a boot loader, which transfers the complete PROM contents into the RAM, changes the program control to the RAM area and switches the power to the PROMs off via transistor switches to conserve power. It then starts monitoring the telecommand interface for possible boot instructions. This allows configuration of the instrument in a flexible, but safe manner. If a start configuration is defined via telecommand, the software continues accordingly. Otherwise, the default start configuration inside the EEPROM is used. If this is corrupted, the original default configuration from PROM is used.

A 512 kByte radiation-hardened EEPROM (Maxwell) contains additional program code and configuration information, which can be modified from the ground. A 2 MByte mass memory RAM stores measurement data and buffers telemetry packets.

An Actel FPGA RT1280 implements the serial data transfer protocol to the IMA detector with an interface identical to the corresponding hardware used on the Rosetta mission. All interface lines are buffered via special circuits to protect the instrument from external noise effects.

The DPU board is controlled by a 24 MHz crystal divided down to 12 MHz and buffered inside an FPGA before it is used for FPGA and processor opera-

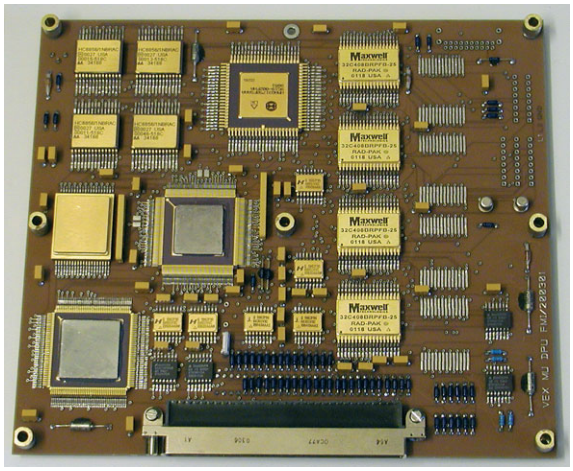

Fig. 35. The main DPU circuit board.

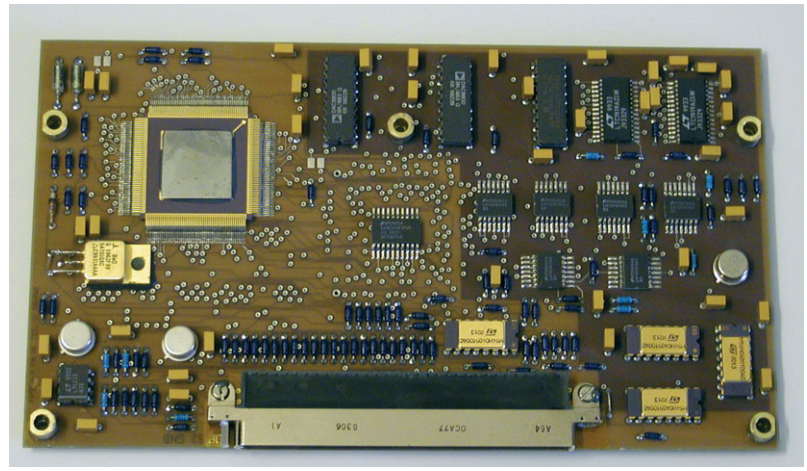

Fig. 36. The ASPERA-4 housekeeping board.

tions and also on the HK board. As the main FPGA needs 2.5 V operations voltage, this is generated by dedicated regulators directly on the DPU and on the HK board. The watchdog circuit inside the FPGA can be enabled by software. Then it has to be reset regularly by software access. Otherwise, it issues a hardware reset to the whole DPU board after 16 s. Except for a special error message, the behaviour is identical to a boot sequence after power-up. The DPU board controls most detector voltages with direct access to the power supply board.

The HK board is controlled by a separate RT54SX32S FPGA, which maps all input and output functions into standard bus address space. It also has the needed counters for detector pulses from NPI and ELS.

Four 8-channel analogue multiplexers select one out of 32 analogue voltages to be monitored. They are digitalised by a 14-bit analogue-to-digital converter (ADC; LTC1419). Another 14-bit ADC monitors the ELS deflection voltage. Two 8-bit digital-to-analogue converters generate via eight latching buffers the control voltages for NPD, NPI, ELS and the scanner. The Sun sensor electronics are also carried on the HK board.

The software is built around a real-time system with scheduler and interrupt handler. All executable routines are defined inside a routing table, which resides in EEPROM and can be modified during flight. In this way, new or modified software routines can be stored inside a free area of the EEPROM, verified and added to the operating software by including their start address into this routing table. A macro feature of the telecommand handler offers the possibility to generate sequences of standard telecommands automatically according to a pre-defined list, reducing the need for complex telecommand groups to be uplinked repeatedly. Besides detector activation and parameter control, compression and averaging of measurement data allow the reduction of the amount of telemetry generated.

2.7 The Scanner

The scanning platform (Fig. 37) was originally developed for ASPERA-C on the Russian Mars-96 project. The modifications made for Mars Express and Venus Express mostly concerned optimisation of the performance during long-term operations and mass reduction. The scanner serves as a bearing structure for ELS, NPI, NPD and the DPU, as well as providing all electrical interfaces with the spacecraft. The technical data of the scanner system are summarised in Table 3.

Fig. 38 shows an internal view of the scanner. The large diameter worm wheel

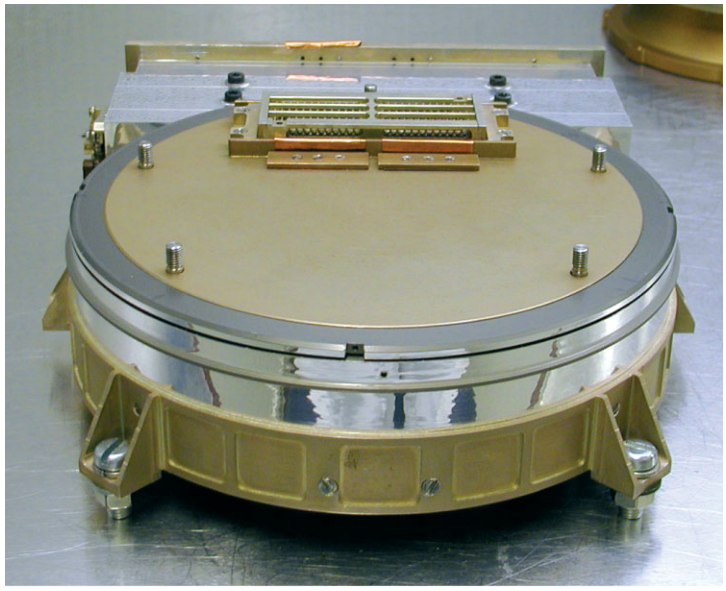

Fig. 37. The ASPERA-4 scanner.

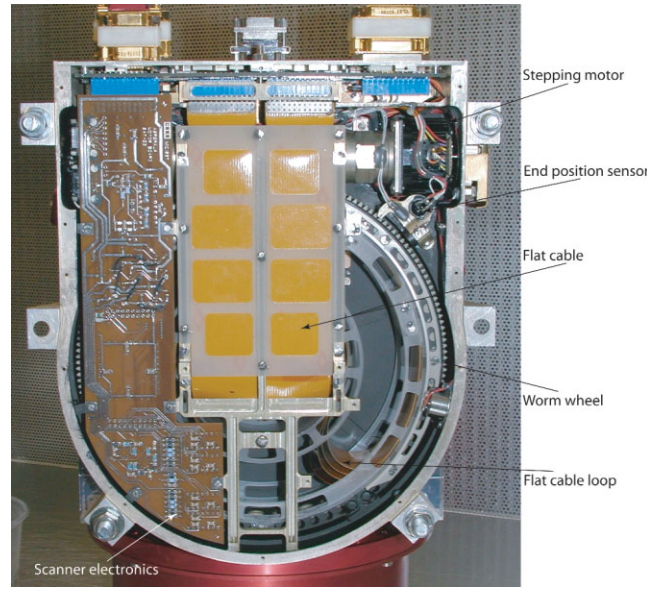

Fig. 38. The Scanner interior with the main features identified.

to which the sensor assembly is fixed is rotated by a stepper motor via a coaxial worm screw (not visible below the flat cable). The worm wheel is fixed to the structure with a large-diameter angular-contact ball bearing. During the scanner life tests, several types of balls, including the ordinary already mounted in the original bearings, were tested. The balls finally used are ceramic (Si_3N_4), which was found to be the most suitable. The housing and circular sensor platform were manufactured in a high-strength aluminium alloy. The motor drive electronics (not shown), also located in the scanner, provide motor control and driving. The position of the movable parts relative the scanner is given by three magnetic sensors, two end-sensors at 0º and 180º, and a step counter. The requirements of long-duration operations mean no mechanical contact in the sensors. The feed-through cable loop with six cables and six connectors, each cable with 26 conductors (a maximum of 156 connections possible) interfacing through D-SUB connectors, provides the electrical interface of the whole instrument with the spacecraft's electrical systems.

A worm gear mechanism was selected to provide self-locking without electrical power, to minimise friction, and to obtain a high gear ratio. The platform was made as a plug-in unit towards the sensor assembly. A great effort was made to reduce mass, volume, power consumption and out-gassing in vacuum, as well as to achieve high reliability. On command, the platform can be turned to an arbitrary position or perform continuous scanning at any rate of rotation up to the maximum. It can also scan in steps; the step angle and duration of each step are programmable.

The scanner carried a locking mechanism to avoid possible movements of the platform during launch vibration. The mechanism contained a wire that tied two small levers locking the worm screw axis. Commanding a voltage to the wire burned it out, allowing a spring to force the levers apart and thus unlock the axis.

3. The Team

The ASPERA-4 experiment involves a large consortium of 16 groups from 11 countries over Europe, USA and Japan. Table 4 shows the primary hardware responsibilities for the different groups. The laboratories thank their sponsoring national agencies, and the departments/institutes hosting these efforts. The

Table 3. Mechanical scanner platform technical data.

Technical data	*Value*
Maximum angle of rotation, °	±100
Angular movement per step, fs. Mode	0.0190
Angular movement per step, hs. Mode	0.0095
Angular position feedback resolution, °	0.05
Angular positioning accuracy, °	0.2
Operational rotation rate, °/s	1.5/3.0/6.0
Maximum rotation rate, °/s	~25.0
Power dissipation, W	0.5–2.0
Platform load, kg	3.7
Maximum platform load, kg	~12
Dimensions, mm x mm x mm	60 x 254 x ?232
Mass, kg	1.42

Table 4. ASPERA-4 groups and primary hardware responsibilities.

Organisation	*Primary hardware contribution*
Swedish Institute of Space Physics, Kiruna, Sweden	PI-institute, Instrument provider NPI, NPD, IMA, scanner provider
Centre d'Etude Spatiale des Rayonnements, Toulouse, France	Co-PI institute, NPI MCPs, IMA anode system, IMA calibrations, IMA development, DC/DC board, scanner driver board, hardware support
Institute of Space and Astronautical Science, Sagamichara, Japan	NPI calibrations and development
University of Bern, Physikalisches Institut, Switzerland	NPD surfaces, NPD mechanics
Instituto di Fisica dello Spazio Interplanetari, Rome, Italy	EGSE, NPI mechanics, NPD electronics
Mullard Space Science Laboratory, UK	ELS calibrations
University of Arizona, Tucson, USA	START surface, NPD UV calibrations
Southwest Research Institute, San Antonio, USA	ELS (MEX spare), data analysis
Rutherford Appleton Laboratory , Oxfordshire, UK	NPD MCPs
Finnish Meteorological Institute, Helsinki, Finland	MU DPU board, MU HK board, IMA DPU board, MU software
Space Physics Research Laboratory, University of Michigan, Ann Arbor, Michigan, USA	Theory
Max Planck Institute for Solar System Research, Katlenburg-Lindau, Germany	NPD TOF electronics
Space Science Laboratory, University of California at Berkeley, Berkeley, California, USA	Theory
Space Research Institute, Graz, Austria	Magnetometer team
Space Technology Ireland, National University of Ireland, Maynooth, Co. Kildare, Ireland	Hardware support
Applied Physics Laboratory/John Hopkins University, Laurel, Maryland, USA	Theory

Principle Investigator Institute (Swedish Institute of Space Physics, Kiruna) acknowledges the Swedish National Space Board for its support.

References

Acuna, M.H., Connerney, J.E.P., Wasilewski, P., Lin, R.P., Anderson, K.A., Carlson, C.W., McFadden, J., Curtis, D.W. Mitchell, D., Reme, H., Mazelle, C., Sauvaud, J.A., d'Uston, C., Cros, A., Medale, J.L., Bauer, S.J., Cloutier, P., Mayhew, M, Winterhalter, D. & Ness, N.F. (1998). Magnetic Field and Plasma Observations at Mars: Initial Results of the Mars Global Surveyor Mission. *Science* **279**, 1676–1680.

Alsop, C., Free, L. & Scott, S. (1996). UV Rejection Design and Performance of the Cluster PEACE 'Top-Hat' Electrostatic Analyser. In *AGU Chapman Conference on Measurement Techniques in Space Plasmas*, AGU Monograph **102**, 269–274.

Barabash, S. (1995). Satellite Observations of the Plasma-Neutral Coupling near Mars and the Earth. *IRF Scientific Report 228*, Swedish Institute of Space Physics, Kiruna, Sweden.

Barabash, S., Lundin, R., Andersson, H., Gimholt, J., Holmström, M., Norberg, O., Yamauchi, M., Asamura, K., Coates, A.J., Linder, D.R., Kataria, D.O., Curtis, C.C., Hsieh, K.C., Sandel, B.R., Fedorov, A., Grigoriev, A., Budnik, E., Grande, M., Carter, M., Reading, D.H., Koskinen, H., Kallio, E., Riihela, P., Säles, T., Kozyra, J., Krupp, N., Livi, S., Woch, J., Luhmann, J., McKenna-Lawlor, S., Orsini, S., Cerulli-Irelli, R., Mura, A., Milillo, A., Roelof, E., Williams, D., Sauvaud, J.-A., Thocaven, J.-J., Winningham, D., Frahm, R., Scherrer, J., Sharber, J., Wurz, P. & Bochsler, P. (2004). ASPERA-3: Analyser of Space Plasmas and Energetic Ions for Mars Express. In *Mars Express: the Scientific Payload*, SP-1240, ESA Publications Division, Noordwijk, The Netherlands, pp121–139.

Biernat, H.K., Erkaev, N.V. & Farrugia, C.J. (1999). Aspects of MHD Flow about Venus. *J. Geophys. Res.* **104**, 12617–12626.

Biernat, H.K., Erkaev, N.V. & Farrugia, C.J. (2000). MHD Effects in the Venus Magnetosheath. *Adv. Space Res.* **26**, 1587–1591.

Biernat, H. K., Erkaev, N.V. & Farrugia, C.J. (2001). MHD Effects in the Venus Magnetosheath including Mass Loading. *Adv. Space Res.* **28**, 833–839.

Brace, L.H., Theis, R.F. & Hoegy, W.R. (1982). Plasma Clouds above the Ionopause of Venus and their Implications. *Planet. Space Sci.* **30**, 29–37, doi:10.1016/0032-0633(82)90069-1.

Brecht, S.H. (1997). Solar Wind Proton Deposition into the Martian Atmosphere. *J. Geophys. Res.* **102**, 11,287–11,294, doi:10.1029/97JA00561.

Carlsson, E., Fedorov, A., Barabash, S., Budnik, E., Grigoriev, A., Gunell, H., Nilsson, H., Sauvaud, J.-A., Lundin, R., Futaana, Y., Holmström, M., Andersson, H., Yamauchi, M., Winningham, J.D., Frahm, R.A., Sharber, J.R., Scherrer, J., Coates, A.J., Linder, D.R., Kataria, D.O., Kallio, E., Koskinen, H., Säles, T., Riihela, P., Schmidt, W., Kozyra, J., Luhmann, J., Roelof, E., Williams, D., Livi, S., Curtis, C.C., Hsieh, K.C., Sandel, B.R., Grande, M., Carter, M., Thocaven, J.-J., McKenna-Lawlor, S., Orsini, S., Cerulli-Irelli, R., Maggi, M., Wurz, P., Bochsler, P., Krupp, N., Woch, J., Fränz, M., Asamura, K. & Dierker, C. (2006). Mass Composition of the Escaping Plasma at Mars, *Icarus* **182**(2), 320–328.

C:son Brandt, P., Barabash, S., Wilson, G.R., Roelof, E.C. & Chase C.J. (2000). Energetic Neutral Atom Imaging at Low (< 10 kev) Energies from Astrid: Observations and Simulations. *J. Atmos. & Solar Terrestrial Phys.* **62**, 901–910.

Donahue, T.M. & Hartle, E. (1992). Solar Cycle Variations in H^+ and D^+ Densities in the Venus Ionosphere: Implications for Escape. *Geophys. Res. Lett.* **12**, 2449–2452.

Fok, M.-C., Moore, T.E., Collier, M.R. & Tanaka, T. (2004). Neutral Atom Imaging of Solar Wind Interaction with the Earth and Venus. *J. Geophys. Res.* **109**(A1), A01206, doi:10.1029/2003JA010094.

Gunell, H., Brinkfeldt, K., Holmström, M., Brandt, P., Barabash, S., Kallio, E., Ekenbäck, A., Futaana, Y., Lundin, R., Andersson, H., Yamauchi, M., Grigoriev, A., Winningham, J.D., Frahm, R.A., Sharber, J.R., Scherrer, J., Coates, A.J., Linder, D.R., Kataria, D.O., Säles, T., Riihela, P., Schmidt, W., Koskinen, H.E.J., Kozyra, J., Luhmann, J., Roelof, E., Williams, D., Livi, S., Curtis, C.C., Hsieh, K.C., Sandel, B.R., Grande, M., Carter, M., Sauvaud, J.-A., Fedorov, A., Thocaven, J.-J., McKenna-Lawlor, S., Orsini, S., Cerulli-Irelli, R., Maggi, M., Wurz, P., Bochsler, P., Krupp, N., Woch, J., Fränz, M., Asamura, K. & Dierker, C. (2006). Measurements and Simulations of Energetic Neutral Atoms Produced by Charge Exchange at Mars. *Icarus* **182**(2), 431–438.

Gunell, H., Holmström, M., Barabash, S., Kallio, E., Janhunen, P., Nagy, A.F. & Ma, Y. (2005a). Planetary ENA Imaging: Effects of Different Interaction Models for Mars. *Planet. & Space Sci.* doi:10.1016/j. pss.2005.04.002.

Gunell, H., Holmström, M., Biernat, H.K. & Erkaev, N.V. (2005b). Planetary ENA Imaging: Venus and a Comparison with Mars. *Planet. & Space Sci.* **53**(4), 433–441, doi:10.1016/j.pss.2004.07.021.

Hartle, R.E. & Grebowsky, J.M. (1990). Upward Ion Flow in Ionospheric Holes on Venus. *J. Geophys. Res.* **95**, 31–37.

Holmström, M., Barabash, S. & Kallio, E. (2001). X-ray Imaging of the Solar Wind-Mars Interaction. *Geophys. Res. Lett.* **28**(7), 1287–1290.

Holmström, M., Barabash, S. & Kallio, E. (2002). Energetic Neutral Atoms at Mars I: Imaging of Solar Wind Protons. *J. Geophys. Res.* **107**(A10), 1277, doi:10.1029/2001JA000325.

Intriligator, D.S., Collard, H.R., Mihalov, J.D., Whitten, R.C. & Wolfe, J.H. (1979). Electron Observations and Ion Flows from the Pioneer Venus Orbiter Plasma Analyzer Experiment. *Science* **205**, 116–119.

Intriligator, D.S., Wolfe, J.H. & Mihalov, J.D. (1980). The Pioneer Venus Orbiter Plasma Analyzer Experiment. *IEEE Transactions on Geoscience and Remote Sensing* **18**, 39–43.

Jans, S. (2000). *Ionization of Energetic Neutral Atoms for Application in Space Instrumentation.* Master's Thesis, Philosophisch-naturwissenschaftlichen Fakultät Universität Bern, Switzerland.

Johnstone, A.D., Alsop, C., Burge, S., Carter, P.J., Coates, A.J., Coker, A.J., Fazakerley, A.N., Grande, M., Gowen, R.A., Gurgiolo, C., Hancock, B.K., Narheim, B., Preece, A., Sheather, P.H., Winningham, J.D. & Woodliffe, R.D. (1997). PEACE: A Plasma Electron and Current Experiment. *Space Sci. Reviews* **79**, 351–398.

Kallio, E. & Barabash, S. (2000). On the Elastic and Inelastic Collisions between Precipitating Energetic Hydrogen Atoms and Martian Atmospheric Neutrals. *J. Geophys. Res.* **105**, 24,973–24,996, doi:10.1029/2000JA900077.

Kallio, E., Luhmann, J.G. & Barabash, S. (1997). Charge Exchange near Mars: The Solar Wind Absorption and Energetic Neutral Atom Production. *J. Geophys. Res.* **102**, 22,183–22,197.

Krasnopolsky, V.A. & Gladstone, G.R. (1996). Helium on Mars: EUVE and Phobos Data and Implications for Mars' Evolution. *J. Geophys. Res.* **101**(A7), 15,765–15,772.

Luhmann, J.G. (1992). Comparative Studies of the Solar Wind Interaction with Weakly Magnetized Planets. *Adv. Space Res.* **12**(9), 191–203.

Luhmann, J.G. & Bauer, S.J. (1992). Solar Wind Effects on Atmosphere Evolution at Venus and Mars. *AGU Geophysical Monograph Series* **66**, 417–430.

Luhmann, J.G. & Kozyra, J.U. (1991). Dayside Pickup Oxygen Ion Precipitation at Venus and Mars – Spatial Distributions, Energy Deposition and Consequences. *J. Geophys. Res.* **96**(15), 5457–5467.

Ma, Y., Nagy, A.F., Hansen, K.C., DeZeeuw, D.L. & Gombosi, T.I. (2002). Three-dimensional Multispecies MHD Studies of the Solar Wind Interaction with Mars in the Presence of Crustal Fields. *J. Geophys. Res.* **107**(A10), 1282, doi:10.1029/2002JA009293.

Marshall, F.J., Hardy, D.A., Huber, A., Pantazis, J., McGarity, J., Holeman, E. & Winningham, J. (1986). Calibration System for Electron Detectors in the Range from 10 eV to 50 keV. *Rev. Sci. Instrum.* **57**(2), 229–235.

McKay, C.P. & Stoker, C.R. (1989). The Early Environment and its Evolution on Mars: Implications for Life. *Rev. Geophys.* **27**, 189–214.

Mihalov, J.D. & Barnes, A. (1982). The Distant Interplanetary Wake of Venus – Plasma Observations from Pioneer Venus. *J. Geophys. Res.* **87**, 9045–9053.

Mihalov, J.D., Wolfe, J.H. & Intriligator, D.S. (1980). Pioneer Venus Plasma Observations of the Solar Wind-Venus Interaction. *J. Geophys. Res.* **85**, 7613–7624.

Moore, K.R., McComas, D.J., Russell, C.T. & Mihalov, J.D. (1990). A Statistical Study of Ions and Magnetic Fields in the Venus Magnetotail. *J. Geophys. Res.* **95**, 12,005–12,018.

Moore, K.R., McComas, D.J., Russell, C.T., Stahara, S.S. & Spreiter, J.R. (1991). Gasdynamic Modeling of the Venus Magnetotail. *J. Geophys. Res.* **96**, 5667–5681.

Nagy, A.F., Cravens, T.E., Yee, J.-H. & Stewart, A.I.F. (1981). Hot Oxygen Atoms in the Upper Atmosphere of Venus. *Geophys. Res. Lett.* **8**, 629–632.

Norberg, O., Yamauchi, M., Lundin, R., Olsen, S., Borg, H., Barabash, S., Hirahara, M., Mukai, M. & Hayakawa, H. (1998). The Ion Mass Imager on the Planet-B Spacecraft. *Earth, Planets & Space* **50**, 199–205.

Russell, C.T., Elphic, R.C. & Slavin, J.A. (1980). Limits on the Possible Intrinsic Magnetic Field of Venus. *J. Geophys. Res.* **85**, 8319–8332.

Sablik, M.J., Scherrer, J.R., Winningham, J.D., Frahm, R.A. & Schrader, T. (1990). TFAS (A Tophat for all Species): Design and Computer Optimization of a New Electrostatic Analyzer. *IEEE Transactions on Geoscience and Remote Sensing* **28**, 1034–1048.

Schubert, G., Russell, C.T. & Moore, W.B. (2000). Timing of the Martian Dynamo. *Nature* **408**, 666–667.

Stewart, A.I.F. (1980). Design and Operation of the Pioneer Venus Orbiter Ultraviolet Spectrometer. *IEEE Transactions on Geoscience and Remote Sensing* **18**, 65–70.

Zhang, T., Baumjohann, W., Delva, M., Auster, H.-U., Balogh, A., Russell, C.T., Barabash, S., Balikhin, M., Berghofer, G., Biernat, H.K., Lammer, H., Lichtenegger, H., Magnes, W., Nakamura, R., Penz, T., Schwingenschuh, K., Vörös, Z., Zambelli, W., Fornacon, K.-H., Glassmeier, K.-H., Richter, I., Carr, C., Kudela, K., Shi, J.K., Zhao, H., Motschmann, U. & Lebreton, J.-P. (2005). Magnetic Field Investigation of the Venus Plasma Environment. *Planet. & Space Sci.* **54**(13/14), 1336–1343.